We are IntechOpen, the world's leading publisher of Open Access books Built by scientists, for scientists

6,900
Open access books available

185,000
International authors and editors

200M
Downloads

Our authors are among the

154
Countries delivered to

TOP 1%
most cited scientists

12.2%
Contributors from top 500 universities



WEB OF SCIENCE™

Selection of our books indexed in the Book Citation Index in Web of Science™ Core Collection (BKCI)

Interested in publishing with us?
Contact book.department@intechopen.com

Numbers displayed above are based on latest data collected.
For more information visit www.intechopen.com



Chapter 10

Solving Inverse Heat Transfer Problems When Using CFD Modeling

Paweł Ludowski, Dawid Taler and Jan Taler

Additional information is available at the end of the chapter

http://dx.doi.org/10.5772/63807

Abstract

The chapter presents solving steady-state inverse heat transfer problems using Computational Fluid Dynamics (CFD) software. Two examples illustrate the application of the proposed method. As the first inverse problem determining the absorbed heat flux to water walls in furnaces of steam boilers is presented in detail. Three different measurement devices (flux tubes) were designed to identify steady-state boundary conditions in water wall tubes of combustion chambers. The first meter is made of a short eccentric tube in which four thermocouples on the fire side below the inner and outer tube surfaces are installed. The fifth thermocouple is situated at the rear of the tube on the housing side of the water wall tube. The second meter has two longitudinal fins that are welded to the bare eccentric tube. In the third option of the instrument, the fins are attached to the water wall tubes but not to the flux tubes as in the second version of the flux tubes. The first instrument is used to measure the heat flux to water walls made from bare tubes, while another two heat flux tubes are designated for measuring the heat flux to membrane walls. Unlike the existing devices, the flux tube is not attached to neighboring water-wall tubes. The absorbed heat flux on the outer surface and the heat transfer coefficient at the inner surface of the flux tube are determined from temperature measurements at internal points. The thermal conductivity of the flux-tube material is a function of temperature. The nonlinear inverse problem of heat conduction (IHCP) is solved using the least-squares method. Three unknown parameters are determined using the Levenberg–Marquardt method. In each iteration, the temperature distribution in the cross section of the heat flux instrument is determined using the ANSYS/CFX software.

Another inverse heat transfer problem will be a CFD simulation carried out for the platen superheater placed in the combustion chamber of the circulating fluidized bed (CFB) boiler. Velocity, pressure, and temperature of the steam, as well as the temperature of the tube wall with the complex cross section, were computed using the ANSYS/CFX software. The direct and inverse problems were solved. In the first inverse problem, the heat transfer coefficient on the flue-gas side was determined based on the meas-

INTECH
open science | open minds

© 2016 The Author(s). Licensee InTech. This chapter is distributed under the terms of the Creative Commons Attribution License (http://creativecommons.org/licenses/by/3.0), which permits unrestricted use, distribution, and reproduction in any medium, provided the original work is properly cited. CC BY

ured steam temperature at the inlet and outlet of the three pass steam superheater. In the second inverse problem, the inlet steam temperature and the heat transfer coefficient on the flue-gas side were estimated using measured steam temperatures at selected locations of the superheater. The Levenberg–Marquardt method was also used to solve the second inverse problem. At every iteration step, a direct conjugate heat transfer problem was solved using the ANSYS/CFX software. The CFX program was called and controlled by an external program written in Python language. The Levenberg–Marquardt algorithm was also included in the Python program.

Keywords: CFD modeling, inverse heat transfer problem, heat flux measurement, pulverized coal-fired boiler, furnace, water wall, circulating fluidized bed boiler, platen superheater

1. Introduction

The aim of direct conjugate heat transfer problems was determining the distribution of pressure, velocity, and temperature of the fluid and solid in the analyzed area when boundary conditions are known. In inverse problems, based on temperature measurements at chosen points located within the analyzed domain, boundary conditions are determined. Nonlinear inverse problems are solved iteratively. At every iteration, the direct problem is solved. When analyzed domain has a complex shape, then it is necessary to apply CFD software to solve the direct problem. In particular, when conjugate boundary problem is solved, that is, when the temperature fields in the liquid and solid are determined simultaneously, use of CFD software becomes indispensable. Two inverse problems are solved in this chapter. Identification of boundary conditions in the tube of membrane water wall was carried out in the first example. The subject of the second inverse problem is to identify the temperature of the steam entering the superheater and the identification of the heat transfer coefficient on the outer surface of the superheater. The Levenberg–Marquardt method was used to solve both inverse problems. At every iteration step, a direct conjugate heat transfer problem was solved using the ANSYS/CFX software. The CFX program was called and controlled by an external program written in Python language. The Levenberg–Marquardt method that was used for solving nonlinear least squares problem was also included in the Python program. This chapter is based mainly on two papers published earlier [1, 2].

2. Measurements of heat flux absorbed by water walls in combustion chambers

Measurements of steady-state heat flux and heat transfer coefficient are subject of many current studies [3–10]. Heat flux measurements absorbed by the water walls of the combustion chamber are used in the design of the steam boilers or in the control systems of the soot blowers. A method for online measurement of the heat flux to the refractory lin-

http://dx.doi.org/10.5772/63807

ing in steam generators of municipal solid waste incinerators is presented in [9, 10]. The heat flux measurement can be used for the online monitoring of the refractory lining as well as for determining the build up of deposits on the membrane walls [9, 10]. Various methods are used for solving inverse heat conduction problem (IHCP) to estimate surface heat flux or heat transfer coefficient. A proper understanding of combustion and heat transfer in furnaces and heat exchange on the water-steam side in tubes needs an accurate measurement of heat flux which is taken over by membrane furnace walls [1, 8–23]. Identification of boundary conditions has also great practical meaning in boiler superheaters [2]. There are three wide categories of heat flux measurements of the boiler water-walls: (1) portable heat flux devices inserted in inspection ports [11–15], (2) Gardon-type heat flux meters welded to the sections of the boiler tubes [11–14], (3) tubular-type instruments located between two neighboring boiler tubes [1, 2, 7, 8, 16–21]. Tubular-type and Gardon meters placed on the furnace tube wall in intense slagging areas can be important boiler diagnostic device for monitoring of slag deposition [2, 22–24]. If a heat flux instrument is to measure the absorbed heat flux accurately, it must be similar to the boiler tube as closely as possible. It is crucial for radiant heat exchange between the flame and measuring instruments. Two main factors in this respect are the emissivity and the temperature of the absorbing surface. Because the instrument will almost always be coated with ash, mainly the properties of the ash and not the instrument dominate the situation. Due to the significant variation of the thermal conductivity, accurate measurements can be performed only if the deposit on the meter is corresponding to that on the surrounding tubes. The tubular-type instruments known also as flux tubes satisfy this requirement. In these devices, the measured heat flux tube temperatures are used for indirect measurement of heat flux.

The measuring tube is equipped with two thermocouples in holes of known radial locations r_1 and r_2. The thermocouples are led out to the junction box where they are connected differentially to give a flux-related electromotive force.

The use of the one-dimensional heat conduction equation for determining temperature distribution in the tube wall gives the simple relationship:

$$q_m = \frac{k(f_1 - f_2)}{r_o \ln(r_1 / r_2)} \tag{1}$$

where f_1 and f_2 are measured wall temperatures at the locations r_1 and r_2, respectively, and r_o is the outer radius of the tube. The symbol k denotes the thermal conductivity of the tube material. The accuracy of this equation is low because of the circumferential heat conduction in the tube wall.

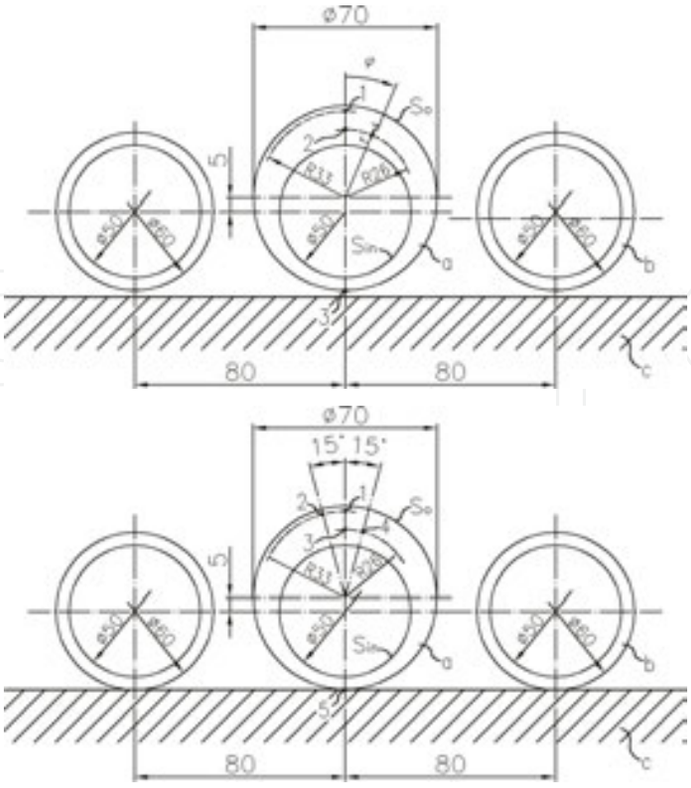


Figure 1. Flux tubes made of bare tubes; (a) flux tube with three temperature sensors, (b) flux tube with five temperature sensors.

Therefore, the measurement of the heat flux absorbed by water-walls with satisfactory accuracy is a challenging task. Considerable work has been done in recent years in this field [1, 2, 9–21, 24]. Previous studies to precisely measure the local heat flux to membrane water walls in steam boilers failed due to unknown water-side heat transfer coefficients. The heat flux can be only determined accurately if the water-side heat transfer coefficient will be identified experimentally [7, 8, 15–18]. In this section, a numerical method for determining the heat flux in boiler furnaces, based on measured interior flux-tube temperatures, is presented. The tubular type device has been designed (**Figures 1** and **2**) to provide a highly accurate measurement of absorbed heat flux q_m, water-side heat transfer coefficient h_f, and water-steam temperature T_f. The number of thermocouples is greater than or equal to three. Unlike existing devices, the developed flux tubes are manufactured from bare or longitudinally finned tubes which are not welded to adjacent water-wall tubes. Temperature distribution in the flux tube is symmetric and not distorted by different temperature fields in neighboring tubes. Significant differences in water temperature can occur in the neighboring water wall tubes of sub- and supercritical once-through boilers due to the nonuniform heat flux distribution across the width of the combustion chamber wall. For this reason, the flux tubes presented in the chapter are especially useful for measurements in the once-through boilers. The thermal conductivity of the flux-tube material depends on temperature. The meter is made from a short piece of the eccentric tube. It contains two or four thermocouples on the fireside below the inner and outer surfaces of the tube. The third (**Figure 1a**) or the fifth thermocouple (**Figures 1b**, **2a**, and **2b**) is

http://dx.doi.org/10.5772/63807

located at the rear of the tube (on the casing side). The boundary conditions on the outer and inner surfaces of the water flux tube must then be determined from temperature measurements at the interior locations. Two (**Figure 1a**) or four (**Figures 1b** and **2**) K-type sheathed thermocouples, 1 mm in diameter, are inserted into holes, which are parallel to the tube axis, that is, parallel to the direction of flow of the water–steam mixture. The end of the sheathed thermocouple, where the hot junction is situated, was bonded to the bottom of the hole using ceramic adhesive to reduce the contact resistance between the thermocouple jacket and tube flux material. The heat transfer by conduction along the thermocouple is minimized because the thermocouples pass through isothermal holes with a depth of 60 mm. The thermocouples are brought to the rear of the tube in the slot machined in the tube wall. An austenitic guard strip with a thickness of 3 mm—welded to the tube—is used to protect the thermocouples from the incident flame radiation. A K-type sheathed thermocouple with a pad is used to measure the temperature at the rear of the flux tube. This temperature is very close to the water-steam temperature. Because the heat flux on the rear surface of the measuring tube is zero (membrane water-walls are perfectly insulated) or very small (bare tube water-walls), the rear part of the tube is almost unheated. For this reason, there is very little difference in temperature between the wall and the fluid in the rear part of the flux tube. This was proved both, by experiments and computer calculations.

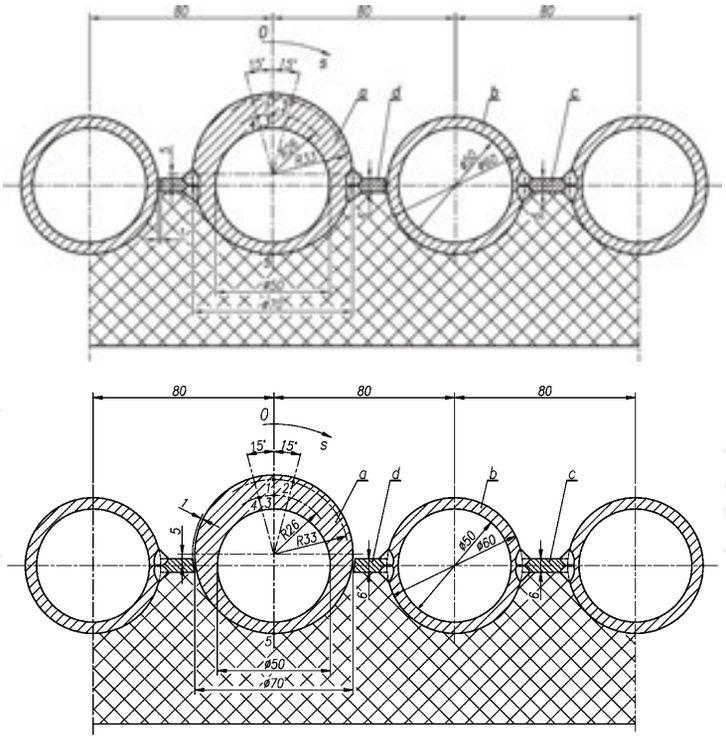


Figure 2. Flux tubes for membrane water walls; (a) fins welded to the flux tube, (b) fins welded to adjacent water wall tubes.

An IHCP was solved using the least squares method. Three unknown parameters were determined using the Levenberg–Marquardt method. At every iteration step, the temperature

distribution in the cross section of the heat flux tube was computed using the ANSYS/CFX software [25]. Test calculations were conducted to estimate the accuracy of the presented method. The uncertainty in determined parameters was calculated using the Gauss uncertainty propagation rule. The technique presented in this chapter is appropriate for water walls made of bare tubes (**Figure 1a** and **b**) and membrane water-walls (**Figure 2a** and **b**). The new technique has advantages in view of the simplicity and accuracy.

The method can be used to determine the resistance of scale or iron oxide on the inner surface of the water wall tubes. The thermal resistance R of deposits on the inner surface of the measuring device can be determined experimentally using the following relationship

$$R = \frac{1}{h_f} - \frac{1}{h_c}, \tag{2}$$

where the symbol h_f stands for the equivalent heat transfer coefficient for the tube inner surface with a scale layer.

The thermal resistance $R_s = \delta_s/k_s$ of the scale layer can be determined analytically, but the thickness δ_s and thermal conductivity k_s of the scale layer are difficult to measure in practice.

The heat transfer coefficient h_c can be identified after the beginning of the boiler operation when the tube inner surface is clean. Also, the value of h_c can be estimated after chemical cleaning of the tube internal surfaces. An equivalent heat transfer coefficient h_f is monitored online during the boiler operation. Another measure of scale presence on the tube inner surface is the maximum temperature of the outer surface of the heat flux tube, which increases with the growth of scale thickness on the inner surface. If the thermal resistance of the scale and the maximum temperature of the heat flux tube is greater than the limit values, the boiler should be cleaned chemically.

2.1. Theory

The water walls can be made of plain tubes or tubes which are welded together with steel flat bars (longitudinal fins) to form membrane wall panels. The water walls are insulated on the rear side and exposed on the front side to radiation from a combustion chamber. The thermometric inserts were manufactured in the laboratory and then securely welded to the water wall tubes at various levels in the combustion chamber of the steam boiler.

The following assumptions in a heat conduction model of the flux tube are made:

- the temperature distribution is two dimensional and steady state,
- the thermal conductivity of the flux tube and membrane wall may depend on temperature,
- the heat transfer coefficient h_c and the scale thickness δ_s are uniform on the inner tube circumference.

The temperature distribution T is governed by the nonlinear partial differential equation

$$\nabla \cdot [k(T)\nabla T] = 0 \tag{3}$$

The unknown boundary conditions may be expressed as

$$\left[k(T)\frac{\partial T}{\partial n} \right]\Big|_{S} = q(s) \tag{4}$$

where $q(s)$ is the radiation heat flux absorbed by the exposed flux tube and membrane wall surface. The local heat flux $q(s)$ is a function of the view factor $\psi(s)$

$$q(s) = q_m \psi(s) \tag{5}$$

where q_m is measured heat flux (thermal loading of the heating surface), and s denotes the coordinate along the boundary (**Figure 2**). The view factor $\psi(s)$ from the infinite flame surface to the differential element on the membrane wall surface ds can be determined graphically [17], or numerically [25].

In this chapter, $\psi(s)$ was evaluated analytically for bare tubes and numerically for membrane water-walls using the finite element program ANSYS/CFX [25] as a function of extended coordinate s.

The boundary condition on the inner surface of the tube S_{in} is defined by Newton's law of cooling

$$-\left[k(T)\frac{\partial T}{\partial n} \right]|_{s_{in}} = h_f (T|_{s_{in}} - T_f) \tag{6}$$

where T_f designates the temperature of the water–steam mixture.

The rear side of the membrane water wall is perfectly insulated. Instead of the boundary condition on the outer surface of the water wall tube, measured values f_i of metal temperature at internal locations of the flux tubes are known

$$T_e(\mathbf{r}_i) = f_i, \quad i = 1, \ldots, m \tag{7}$$

where $m = 3$ or $m = 5$ designates the number of thermocouples (**Figures 1** and **2**). The unknown parameters: $x_1 = q_m$, $x_2 = h_f$, and $x_3 = T_f$ were estimated using the least-squares method. The symbol $r_{in} = d_f/2 = d_t/2$ stands for the inner tube radius. The symbols d_f and d_t designate the inner diameter of the flux and water wall tube, respectively. Unknown parameters $\mathbf{x} = (x_1, \ldots, x_n)^{\mathrm{tr}}$ for $n = 3$ are selected so that computed temperatures $T(\mathbf{x}, \mathbf{r}_i)$ agree within certain limits with

the experimentally measured temperatures f_i. The location of the thermocouple is defined by the position vector $\mathbf{r}_i$. This may be expressed as

$$T(\mathbf{x},\mathbf{r}_i) - f_i \cong 0, \quad i = 1,\ldots,m. \tag{8}$$

The least-squares method is used to determine parameters $\mathbf{x}$. The sum of squares

$$S(\mathbf{x}) = \sum_{i=1}^{m} [f_i - T(\mathbf{x},\mathbf{r}_i)]^2 \tag{9}$$

can be minimized by a general unconstrained method.

However, the properties of (9) make it worthwhile to use methods designed specifically for the nonlinear least-squares problem. In this work, the Levenberg–Marquardt method [26, 27] is used to determine the parameters x_1, x_2 and x_3. The Levenberg–Marquardt method performs the k-th iteration as

$$\mathbf{x}^{(k+1)} = \mathbf{x}^{(k)} + \delta^{(k)} \tag{10}$$

where

$$\boldsymbol{\delta}^{(k)} = [(\mathbf{J}^{(k)})^{tr}\mathbf{J}^{(k)} + \mu\mathbf{I}_{\mathbf{n}}]^{-1}(\mathbf{J}^{(k)})^{tr}[\mathbf{f} - \mathbf{T}(\mathbf{x}^{(k)})], \quad k = 0,1,\ldots \tag{11}$$

where μ is the multiplier, and I_n is the identity matrix. The Levenberg–Marquardt method is a combination of the Gauss–Newton method ($\mu^{(k)} \to 0$) and the steepest-descent method ($\mu^{(k)} \to \infty$). The latter method is used far from the minimum, changing continuously to the former as the minimum is approached. Initially, a small positive value of μ was selected, for example, $\mu^{(1)} = 0.01$. If, at the kth iteration, the step $\boldsymbol{\delta}^{(k)}$ of (10) reduces S($\mathbf{x}$), then $\mu^{(k)}$ is decreased by a factor of 10 and trial solution is updated, that is, $\mathbf{x}^{(k+1)} = \mathbf{x}^{(k)} + \boldsymbol{\delta}^{(k)}$. In this way, the algorithm is pushed closer to Gauss–Newton method. If within the kth iteration, the step $\boldsymbol{\delta}^{(k)}$ does not reduce S($\mathbf{x}$), $\mu^{(k)}$ is progressively increased by a factor of 10, for example, $\mu^{(k)} = 10\mu^{(k)}$, each time recomputing $\boldsymbol{\delta}^{(k)}$ until a reduction in S($\mathbf{x}$) is achieved. The $m \times n$ Jacobian matrix $\mathbf{J}$ of $T(\mathbf{x}^{(k)}, \mathbf{r}_i)$ is defined as

http://dx.doi.org/10.5772/63807

$$\mathbf{J}^{(k)} = \frac{\partial \mathbf{T}(\mathbf{x})}{\partial \mathbf{x}^{tr}}\Big|_{\mathbf{X}=\mathbf{X}^{(k)}} = \left[\begin{array}{ccc} \frac{\partial T_1}{\partial x_1} & \cdots & \frac{\partial T_1}{\partial x_n} \\ \cdots & \cdots & \cdots \\ \cdots & \cdots & \cdots \\ \cdots & \cdots & \cdots \\ \cdots & \cdots & \cdots \\ \frac{\partial T_m}{\partial x_1} & \cdots & \frac{\partial T_m}{\partial x_n} \end{array}\right]_{\mathbf{X}=\mathbf{X}^{(k)}}, \tag{12}$$

where $\mathbf{T}(\mathbf{x}^{(k)}) = (T_1{}^{(k)}, \ldots, T_m{}^{(k)})^{\mathrm{tr}}$. A finite-difference method was used to estimate the Jacobian matrix at the approximate solution. The sensitivity coefficient defined in Eq. (12) is important indicators of the ability to estimate the unknown parameters. Very small sensitivities indicate the parameters difficult to estimate. The inverses of the sensitivities appear in the variance propagation rule given by Eq. (16). Although the unknowns x_1, x_2, and x_3, are not of the same order of magnitude, the normalized and not normalized vector **x** gave the same solutions. Therefore, the vector **x** was not normalized prior to the solution of the problem. The iterative procedure is continued until the variations in $x_i{}^{(k)}$, $i = 1, \ldots, n$ are less than a small preset tolerance ε. At every k-th iteration step, the temperature distribution $\mathbf{T}(\mathbf{x}^{(k)}, \mathbf{r}_i)$ is calculated using the element-based FVM method.

The estimates for the initial values of the parameters $x_1{}^{(1)}$, $x_2{}^{(1)}$, and $x_3{}^{(1)}$ are

$$x_1^{(1)} = \frac{k^{(1)}}{r_o}\frac{0.5(f_1+f_2)-0.5(f_3+f_4)}{\ln(r_1/r_2)} \tag{13}$$

$$x_2^{(1)} = \frac{x_1^{(1)} r_o}{r_{in}}\frac{1}{0.5(f_3+f_4)-(x_1^{(1)} r_o/k^{(1)})\ln\{r_2/[r_2-0.8(r_2-r_{in})]\}-x_3^{(1)}} \tag{14}$$

$$x_3^{(1)} = f_5 \tag{15}$$

where the radii are: $r_o = 0.035$ m, $r_{in} = 0.020$ m, $r_1 = 0.033$ m, $r_2 = 0.026$ m. The thermal conductivity $k^{(1)}$ is evaluated at the mean temperature:

$$f_m = (f_1 + f_2 + f_3 + f_4)/4, i.g.k^{(1)} = k(f_m).$$

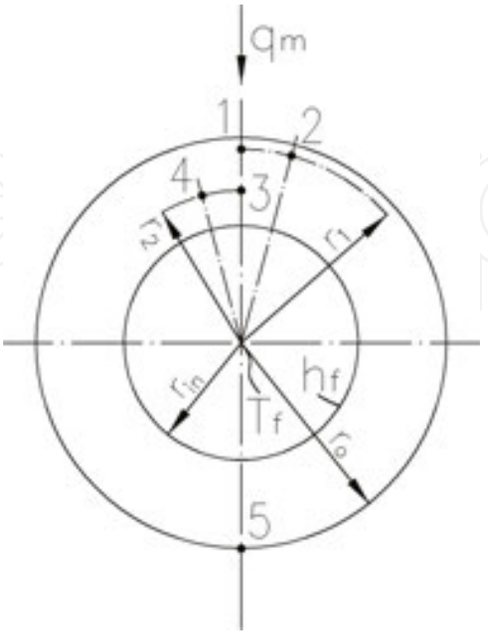


Figure 3. Flux tube with constant thickness used to determine initial values of unknown sought parameters.

The relationships (13)–(15) were derived assuming one-dimensional temperature distribution in the heat flux tube with constant thickness (**Figure 3**). In the formula (14), the tube wall temperature at the distance: 0.2 ($r_2 - r_{in}$) from the inner surface was taken as the temperature of the tube inner surface, which results in a lower initial value of the heat transfer coefficient $x_2^{(1)}$.

The Levenberg–Marquardt method allows determining the desired parameters even for an inaccurate estimation of their starting values since the steepest-descent method is used at the beginning of the iteration process. The use of Eqs. (13–15) to select the initial values of parameters makes it possible to find quickly a convergent solution with a small number of iterations. By selecting other starting values, the correct solution is also obtained but with a larger number of iterations.

The Levenberg–Marquardt method works very well in practice and has become the standard of nonlinear least-squares procedures [26, 27]. The boundary value problem that is given by Eq. (3) and boundary conditions (4) and (6) was solved at each iteration step by the element based finite volume method using the ANSYS/CFX software. The CFX program was called and controlled by an external program written in Python programming language [28]. The Levenberg–Marquardt algorithm was also incorporated into the Python program.

2.2. Uncertainty analysis

The uncertainties of the determined parameters $\mathbf{x}^*$ will be estimated using the error propagation rule of Gauss [29–33]. The propagation of uncertainty in the independent variables:

http://dx.doi.org/10.5772/63807

measured wall temperatures f_j, $j = 1, \ldots, m$, thermal conductivity k, radial r_j and angular ϕ_j, $j = 1, \ldots, m$, coordinates of the thermocouples is estimated from the following expression

$$2\sigma_{x_i} = \left\{ \sum_{j=1}^{m} \left[\left(\frac{\partial x_i}{\partial f_j} 2\sigma_{f_j} \right)^2 + \left(\frac{\partial x_i}{\partial r_j} 2\sigma_{r_j} \right)^2 + \left(\frac{\partial x_i}{\partial \varphi_j} 2\sigma_{\varphi_j} \right)^2 \right] + \left(\frac{\partial x_i}{\partial k} 2\sigma_k \right)^2 \right\}^{\frac{1}{2}}, \quad i = 1,2,3. \tag{16}$$

The symbols, $\sigma_{f_j}^2$, $\sigma_{r_j}^2$, $\sigma_{\varphi_j}^2$, and σ_k^2 designate variances of measured temperatures, radial, and angular thermocouple locations and thermal conductivity.

The 95% uncertainty in the estimated parameters can be expressed in the form $x_i = x_i^* \pm 2\sigma_{x_i}$, where $x_i = x_i^*$, $i = 1, 2, 3$ represent the value of the parameters obtained using the least squares method.

The sensitivity coefficients $\partial x_i/\partial f_j$, $\partial x_i/\partial r_j$, $\partial x_i/\partial \phi_j$, and $\partial x_i/\partial k$ in Eq. (16) were approximated by the central difference quotients

$$\frac{\partial x_i}{\partial f_j} = \frac{x_i(f_1,\ldots,f_j+\delta,\ldots,f_m) - x_i(f_1,\ldots,f_j-\delta,\ldots,f_m)}{2\delta}, \quad i = 1,\ldots,n, \qquad j = 1,\ldots,m \tag{17}$$

where δ is a small positive number.

The error propagation rule given by Eq. (16), which is also known as the principle of the variance propagation, is used extensively to assess the uncertainty of indirect steady-state measurements.

2.3. Test computations

Four thermometric inserts will be investigated. In the first flux tube (**Figure 1a**) made from a plain eccentric tube, the wall temperature is measured at two locations at different radii on the fire side. The third thermocouple is placed on the outer tube surface on the insulated side of the water wall. In the second flux tube (**Figure 1b**), made also from the bare tube, four thermocouples are placed at the forward tube part. The fifth temperature sensor is situated at the same position as in the first heat flux. The third flux tube (**Figure 2a**) has two longitudinal fins, which are not welded to the adjacent water wall tubes, so the temperature distribution in the measuring device is not disturbed by the water wall tubes. The fourth device (**Figure 2b**)

is without fins, which are welded to the neighboring water wall tubes. There are four thermocouples located at different radii and angles in the flux-tube wall on the fire side, and one thermocouple is attached to the outer tube surface on the back side of the water wall.

2.3.1. Flux tube made from bare tube

First, the temperature distribution in the cross section of the flux tube will be determined. The following data were adopted for the calculation: absorbed heat flux, $q_{m,e}$ = 250 000 W/m^2, heat transfer coefficient, $h_{f,e}$ = 30 000 W/(m^2 K), and the temperature of the water-steam mixture, $T_{f,e}$ = 318°C. The view factor $\psi(\phi)$ was evaluated analytically and numerically using the ANSYS software. The consistency of analytical and numerical results is quite good (**Figure 4**).

Temperature, °C	100	200	300	400
Thermal conductivity, W/(m K)	50.69	48.60	46.09	42.30

Table 1. Thermal conductivity k(T) of steel 20G, as a function of temperature.

The view factor at φ = 180° is about 0.08 since a part of the incident radiation heat flux from the combustion chamber passes through spaces between bare tubes and is reflected by the adiabatic boiler refractory. The material of the heat flux tube is 20G steel. The composition of the 20G mild steel is as follows: 0.17–0.24% C, 0.7–1.0% Mn, 0.15–0.40% Si, 60.04% P, 60.04% S. The thermal conductivity of the heat flux tube is assumed to be temperature dependent (**Table 1**).

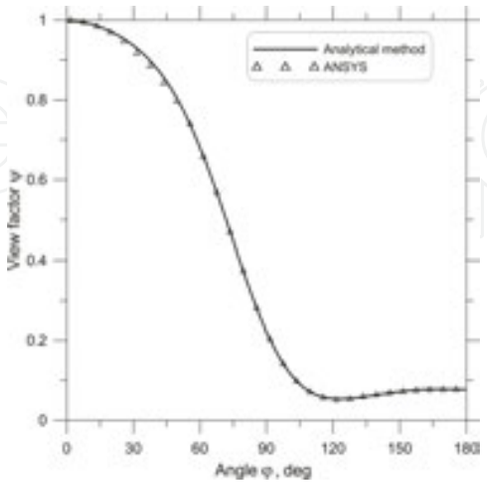


Figure 4. Comparison of view factor calculated analytically and numerically using ANSYS/CFX for the flux tubes shown in **Figure 1**. The origin of the cylindrical coordinate system is at the center of the outer flux-tube surface.

The 95% uncertainty interval for thermal conductivity was assumed ±0.5 W/(m K) [34]. The thermal conductivity of the flux-tube material (mild steel 20G) was approximated using a simple linear function

$$k(T) = 53.26 - 0.0238T \tag{18}$$

First, measured temperatures were generated artificially to test the method developed in the chapter. The division of the flux-tube model into finite elements is shown in **Figure 5**. Three different finite element meshes were used to compute the temperature at the locations 1–5. The temperature distribution in the flux tube was calculated using ANSYS/CFX v13.0.

The coordinates of the temperature measuring points 1–5 are as follows:

P_1	$r_1 = 33$ mm, $\phi_1 = 0°$,
P_2	$r_2 = 33$ mm, $\phi_2 = 15°$,
P_3	$r_3 = 26$ mm, $\phi_3 = 0°$,
P_4	$r_4 = 26$ mm, $\phi_4 = 15°$,
P_5	$r_5 = 35$ mm, $\phi_5 = 180°$,

The temperature at the points 1–5 obtained for various meshes shown in **Figure 5** are summarized in **Table 2**.

The analysis of the results listed in **Table 2** shows that the temperature calculated using the different grids are very close to each other.

Measuring point	**Temperature, °C**	**Finite element mesh**		
		Figure 5a	**Figure 5b**	**Figure 5c**
1	T_1	418.31	418.36	418.55
2	T_2	415.66	415.77	415.84
3	T_3	374.08	373.75	374.14
4	T_4	372.22	372.17	372.22
5	T_5	321.11	321.10	321.12

Table 2. Flux-tube temperature at the points P_1–P_5 computed for different finite element meshes shown in **Figure 5**.



Figure 5. Division of geometrical model of the heat flux tube into finite elements; (a) hexahedral mesh–1150 elements hex8, 1692 nodes; (b) tetrahedral mesh—1909 elements tet4, 518 nodes; (c) hexahedral mesh—59520 elements hex8, 66759 nodes.

http://dx.doi.org/10.5772/63807

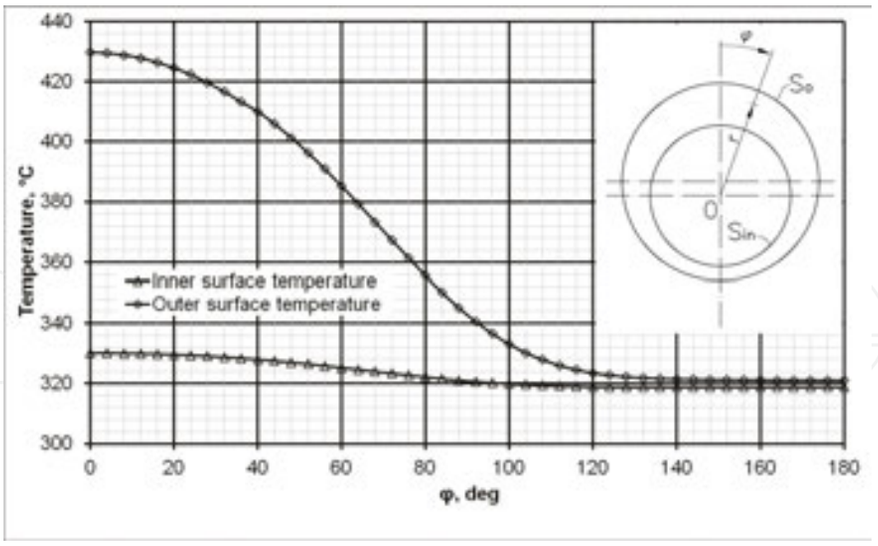


Figure 6. Flux-tube temperature at the outer and inner surfaces as a function of angular coordinate φ_1.

The temperature changes at the inner and outer surface on the flux-tube circumference which were obtained using the mesh shown in **Figure 5a** are depicted in **Figure 6**.

First, the temperatures for the mesh shown in **Figure 5a** were taken as "measured data": f_1 = 418.31°C, f_2 = 415.66°C, f_3 = 374.08°C, f_4 = 372.22°C, f_5 = 321.11°C (**Table 2**).

Taking the calculated temperatures as measured temperatures and using the same finite element mesh, the following results are obtained:

- For three measuring points: P_1, P_3, and P_5 (**Figure 1a**):

$$q_m = 250000.19\,\mathrm{W/m^2},$$

$$h = 30000.38\,\mathrm{W/(m^2\ K)},$$

$$T_f = 318.00°\mathrm{C}$$

- For five measuring points: P_1, P_2, P_3, P_4, and P_5 (**Figure 1b**):

$$q_m = 249999.94\,\mathrm{W/m^2},$$

$$h = 30000.16\,\mathrm{W/(m^2\ K)},$$

$$T_f = 318.00°\mathrm{C}.$$

When the temperature values obtained for the mesh illustrated in **Figure 5c** were adopted as "measured data" then an inverse calculation using the mesh shown in **Figure 5a** gives little different results:

- For three measuring points: P_1, P_3, and P_5 (**Figure 1a**):

$$q_m = 250892.94 / \mathrm{m}^2,$$

$$h = 30418.33 / (\mathrm{m}^2\ \mathrm{K}),$$

$$T_f = 318.00°\mathrm{C}.$$

- For five measuring points: P_1, P_2, P_3, P_4, and P_5 (**Figure 1b**):

$$q_m = 250898.22\ \mathrm{W/m}^2,$$

$$h = 30498.66\ \mathrm{W/(m}^2\cdot\mathrm{K}),$$

$$T_f = 318.01°\mathrm{C}.$$

Analysis of the results demonstrates that for exact "measurement data," the obtained results are in very good agreement with the input values. The impact of measuring point number on the results of the inverse problem solution can be better estimated when the measured temperatures are assumed to be disturbed with pseudorandom errors, which are characterized by the 95% uncertainty intervals: $2\sigma_{f_j} = \pm 0.2\ K; 2\sigma_{r_j} = \pm 0.05\ mm; 2\sigma_{\varphi_j} = \pm 0.5$, j = 1, …, 5; $2\sigma_k = \pm 0.5\ W/(m \cdot K)$. At first, the uncertainties in the estimated parameters: $x_1 = q_m$, $x_2 = h$, $x_3 = T_f$ will be determined when the flux tube illustrated in **Figure 1a** is used. To estimate uncertainties in determined parameters, Eq. (16) was used. The partial derivatives appearing in Eq. (16) were calculated using the central difference approximation (17). The results are listed in **Table 3**.

The analysis of the results presented in **Table 3** shows that the largest absolute values have the following coefficients: $\partial q_m/\partial f_j$, $\partial h_f/\partial f_j$, $\partial q_m/\partial r_j$, and $\partial h_f/\partial r_j$.

For this reason to obtain small uncertainties in the heat flux q_m and the heat transfer coefficient h_f, the random errors in measured temperatures and radial locations of the thermocouples should be small.

Applying Eq. (16) yields: $2\sigma_{(x1)}$= 4073.50 W/m2; $2\sigma_{(x2)}$= 3921.12W/(m2·K); $2\sigma_{(x3)}$= 0.22 K. The 95% uncertainties in the estimated parameters are as follows:

http://dx.doi.org/10.5772/63807

$$q_m = 250000.2 \pm 4073.5\ \mathrm{W/m^2},$$

$$h_f = 30000.4 \pm 3921.1\ \mathrm{W/(m^2 \cdot K)},$$

$$T_f = 318.0 \pm 0.22\ ^\circ\mathrm{C}.$$

Thermocouple number, j	$\partial x_i/\partial f_j$		
	$\partial q_m/\partial f_j$, **W/(m²K)**	$\partial h_f/\partial f_j$, **W/(m²K²)**	$\partial T_f/\partial f_j$ **–**
1	2825.19	1656.70	−0.0018
2	2663.14	1589.09	0.0179
3	−2718.39	−3037.09	−0.0536
4	−2784.89	−3019.57	−0.0342
5	−119.11	2798.77	1.0722
Thermocouple number, j	$\partial x_i/\partial r_j$		
	$\partial q_m/\partial r_j$, **W/(m²·mm)**	$\partial h_f/\partial r_j$, **W/(m²·K·mm)**	$\partial T_f/\partial r_j$, **K/mm**
1	−16347.09	−9468.39	0.0143
2	−15136.96	−8846.43	−0.1046
3	18012.69	27039.19	0.3659
4	18156.25	26298.52	0.2319
5	51.72	−1268.71	−0.4674
Thermocouple number, j	$\partial x_i/\partial \phi_j$		
	$\partial q_m/\partial \phi_j$, **W/(m²·deg)**	$\partial h_f/\partial \phi_j$, **W/(m²·K·deg)**	$\partial T_f/\partial \phi_j$, **K/deg**
1	114.55	133.76	−0.0002
2	−1104.76	−670.19	−0.0079
3	−134.66	−150.88	−0.0027
4	768.36	812.51	0.0090
5	−0.24	0.88	0.0004
	$\partial x_i/\partial k$		
	$\partial q_m/\partial k$, **K/m**	$\partial h_f/\partial k$, **1/m**	$\partial T_f/\partial k$, **m·K²/W**
	5696.11	742.42	−0.0006

Table 3. Partial derivatives appearing in Eq. (16) for the evaluation of measurement uncertainty.

If the device with five temperature measurement points is used (**Figure 1b**) then the uncertainties become smaller: $2\sigma_{x_1} = 3557.73\,\mathrm{W/m^2}; 2\sigma_{x_2} = 2379.85\mathrm{W/(m^2K)}; 2\sigma_{x_3} = 0.22\,\mathrm{K}$.

The limits of the 95% uncertainty interval are as follows:

$$q_m = 249999.9 \pm 3557.7\,\mathrm{W/m^2},$$

$$h_f = 30000.16 \pm 2379.9\,\mathrm{W/(m^2\ K)},$$

$$T_f = 318.0 \pm 0.22°\mathrm{C}.$$

Inspection of the results demonstrates the good accuracy in both cases. If the number of temperature measurement points is equal five then the uncertainties in the estimated heat flux and heat transfer coefficient become smaller, because an imprecise location of one thermocouple has a smaller influence on the estimated parameters. For two temperature sensors placed at the forward part of the heat flux tube, an inaccurately situated temperature sensor influences to a larger extent the results.

If the standard deviations of the variables measured directly are greater also standard deviations of the determined parameters: q_m, h_f, and T_f will be greater. If the random errors will be doubled, the standard deviation will also be doubled. This conclusion follows from the analysis of Eq. (16). This has no effect on the convergence of the solution. For larger random errors in measured temperatures, a convergent solution is obtained, but with a slightly larger number of iterations.

To demonstrate the influence of the selection of parameter initial values on the solution convergence and on the number of iterations, the computations will be carried out for five measuring temperature points and using two sets of initial values:

- $q_m^{(1)} = 100\ 000\ \mathrm{W/m^2}$, $h_f^{(1)} = 40\ 000\ \mathrm{W/(m^2\ K)}$, $T_f^{(1)} = 316°\mathrm{C}$,
- $q_m^{(1)} = 400\ 000\ \mathrm{W/m^2}$, $h_f^{(1)} = 10\ 000\ \mathrm{W/(m^2\ K)}$, $T_f^{(1)} = 317°\mathrm{C}$,

Adopting "measured data" from **Table 2** for the mesh shown in **Figure 5a**, the following results were obtained:

- $q_m = 249999.80\mathrm{W/m^2}$, $h_f = 29999.78\mathrm{W/(m^2K)}$, $T_f = 318.00°\mathrm{C}$ after 27 iterations,
- $q_m = 250000.15\mathrm{W/m^2}$, $h_f = 30000.03\mathrm{W/(m^2K)}$, $T_f = 318.00°\mathrm{C}$ after 27 iterations.

Because the start values of parameters are far from the input values (exact solution) the number of iteration is large. However, the solution found is correct in both cases.

If one of the temperature measurements is affected by a significant measurement error then the incorrect temperature measurement must be removed from the analysis. It was

assumed that the measured temperature at the point 4 is equal to the measured temperature at the point 5 to assess the influence of the large measurement error. Using the finite element mesh depicted in **Figure 5a** and disturbed "measurement data": f_1 = 418.31°C, f_2 = 415.66°C, f_3 = 374.08°C, f_4 = 321.11°C, f_5 = 321.11°C, the following values of the parameters were found: q_m = 303 248.29 W/m^2, h_f = 5 705 392.54 W/(m^2 K), T_f = 306.16°C. One can see that the determined parameters considerably differ from the exact values: q_m = 250 000 W/m^2, h_f = 30 000 W/(m^2 K), T_f = 318°C. In practice, it is easy to notice that one of the measuring points is damaged because during correct measurements the temperatures measured at the points 1 and 2 should be similar, as well as temperatures at the points 3 and 4 should be close to each other.

2.3.2. Flux tube for membrane water walls–fins attached to the flux tube

In combustion chambers with membrane water walls, heat flux tube with longitudinal fins may be used (**Figure 2a**). To eliminate the influence of neighboring water wall tubes on the temperature field in the heat flux tube, the longitudinal fins are not welded to the adjacent tubes.

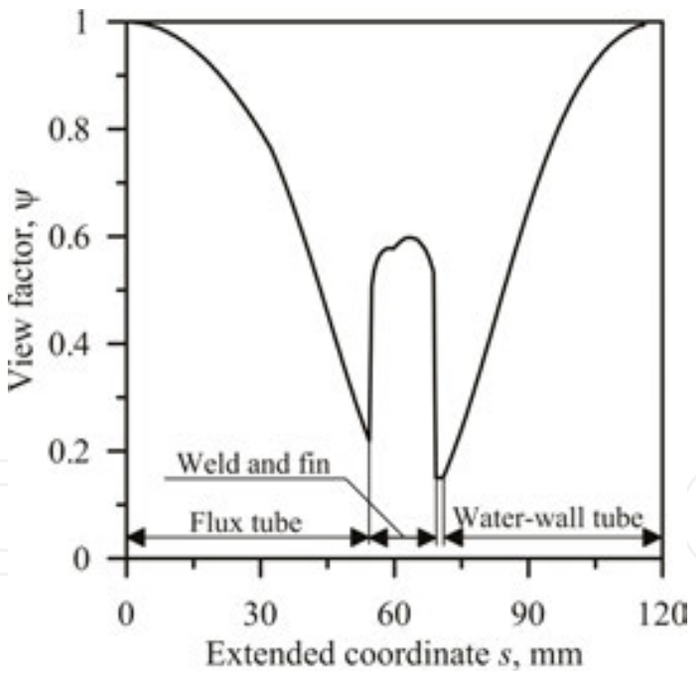


Figure 7. View factor distribution on the outer surface of the flux tube and adjacent water-wall tube which are shown in **Figure 2a**.

The distribution of the view factor on the surface of the flux tube, fin, and water wall tube is depicted in **Figure 7**. The origin of the s coordinate is shown in **Figure 2**. Because of the symmetry, only the representative water wall section illustrated in **Figure 8** needs to be analyzed.

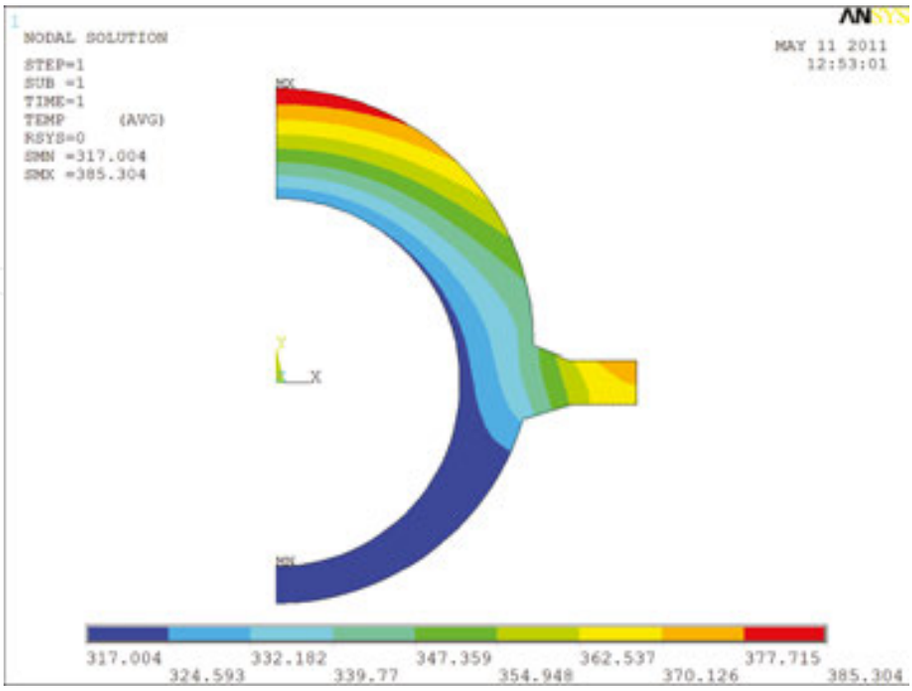
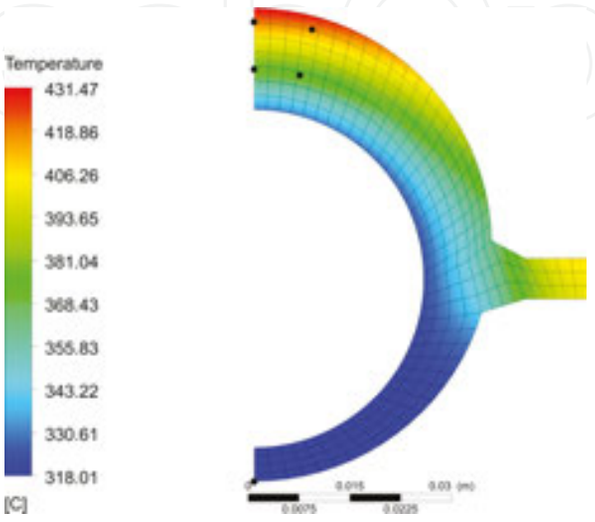


Figure 8. Temperature distribution in the flux-tube cross section for: q_m = 150000 W/m^2. T_f = 317°C and h_f = 27000 W/(m^2 K).

To illustrate that the maximum temperature of the fin tip is lower than the allowable temperature for the 20G steel, the flux-tube temperature was calculated using ANSYS/CFX package [25]. Variations of the view factor on the flux-tube weld and fin surface were also calculated with ANSYS/CFX. An inspection of the results shown in **Figure 8** shows that the maximum temperature of the fin does not exceed 375°C. Next to illustrate the effectiveness of the presented method test calculations were carried out. The thermal conductivity of the 20G steel was approximated by the function (18).



http://dx.doi.org/10.5772/63807

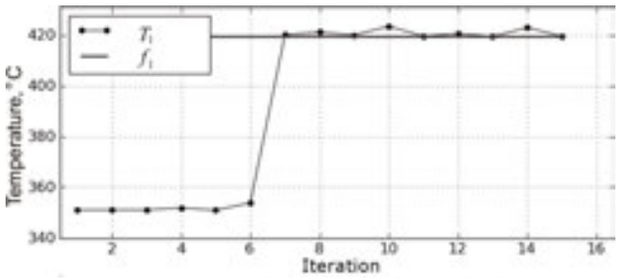


Figure 9. Temperature distribution (a) in the flux tube obtained from the solution of the inverse problem for the "exact" data: f1 = 419.66°C. f2 = 417.31°C. f3 = 374.90°C. f4 = 373.19°C. f5 = 318.01°C and iteration number (b) for the temperature T1.

The "measured" temperatures f_i, $i = 1, 2, \ldots, 5$ were generated artificially by means of ANSYS/CFX for: q_m = 250 000 W/m^2, h_f = 30 000 W/(m^2 K) and Tf = 318°C. The following values of "measured" temperatures were obtained $f_1 = 419.66$°C, $f_2 = 417.31$°C, $f_3 = 374.90$°C, $f_4 = 373.19$°C, $f_5 = 318.01$°C. The temperature distribution in the flux-tube cross section reconstructed on the basis of five measured temperatures is shown in **Figure 9a**. The inverse method presented in the chapter is very accurate because the estimated parameters:
$q_m = 250\,000.063$ W/m^2, $h_f = 30\,000.054$ W/(m^2 K), and $T_f = 318.0$°C differ slightly from the input values.

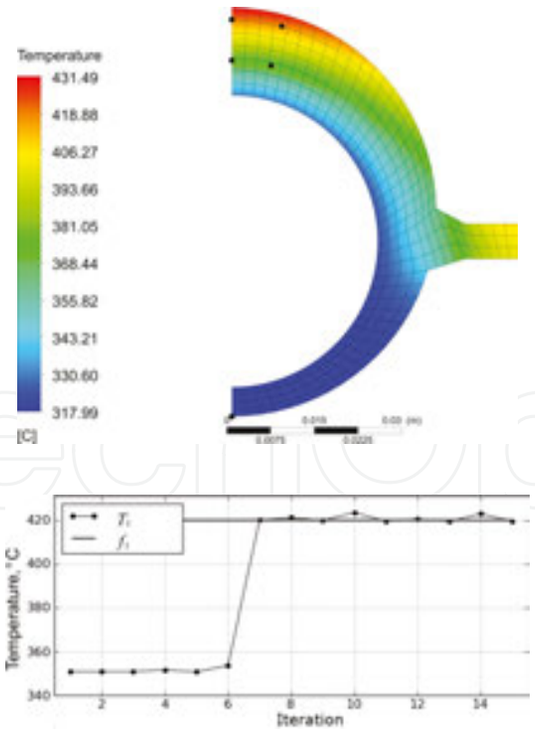


Figure 10. Temperature distribution (a) in the flux tube obtained from the solution of the inverse problem for the "perturbed" data: f_1 = 420.16°C. f_2 = 416.81°C. f_3 = 375.40°C. f_4 = 372.69°C. f_5 = 318.01°C and iteration number (b) for the temperature T_1.

To show the influence of the measurement errors on the determined parameters, the 95% confidence intervals were estimated. The following uncertainties of the measured values were assumed (at 95% confidence interval): $2\sigma_{f_j} = \pm 0.4\text{K}$, $2\sigma_{r_j} = \pm 0.10\text{mm}$, $2\sigma_{\varphi_j} = \pm 1.0°$, $j=1, \ldots, 5$, $2\sigma_k = \pm 1.0\text{W}/(\text{mK})$. For these test calculations, the 95% uncertainties in the parameters measured directly were taken two times greater than the uncertainties in the previous case analyzed in Section 4.1. The limits of the 95% uncertainty interval are as follows:

$$q_m = 250000.06 \pm 7102.46\ \text{W/m}^2,$$

$$h_f = 30000.05 \pm 4735.71\ \text{W/(m}^2\ \text{K)},$$

$$T_f = 318.00 \pm 0.41°\text{C}.$$

Despite the doubling of uncertainties, the results are quite good. Larger relative errors in determined the heat transfer coefficient are due to a small difference in temperature between the inner surface of the flux tube and the fluid temperature. For this reason, the impact of the uncertainties in direct measurements on the estimated heat transfer coefficient is greater.

The uncertainties (95% confidence interval) of the coefficients x_i were determined using the error propagation rule (16). The calculated uncertainties are: ±4.1% for q_m, ±27.3% for h_f and ±0.1% for T_f. The accuracy of the results obtained is acceptable.

Then, the inverse analysis was carried out for perturbed data: $f_1 = 420.16°\text{C}$, $f_2 = 416.81°\text{C}$, $f_3 = 375.40°\text{C}$, $f_4 = 372.69°\text{C}$, $f_5 = 318.01°\text{C}$. The reconstructed temperature distribution is illustrated in **Figure 10a**. The obtained results are $q_m = 250\ 118.613\ \text{W/m}^2$, $h_f = 30\ 050.041\ \text{W/(m}^2\ \text{K)}$ and $T_f = 317.99°\text{C}$. The influence of the error in the measured temperatures on the estimated parameters is small.

The number of iterations in the Levenberg–Marquardt procedure is small in both cases (**Figures 9b** and **10b**).

2.4. Flux tube for membrane water walls—fins attached to the adjacent water wall tubes

The variation of the view factor on the surface of the flux tube, fin, and water wall tube is illustrated in **Figure 11**. The origin of the cylindrical coordinate system is at the center of the outer flux-tube surface (**Figure 2b**). Because of the symmetry, only the half of the flux tube was considered.

The measured temperatures: $f_1 = 418.28°\text{C}$, $f_2 = 415.61°\text{C}$, $f_3 = 374.05°\text{C}$, $f_4 = 372.18°\text{C}$, $f_5 = 318.00°\text{C}$ were generated artificially for the following input data $q_m = 250\ 000\ \text{W/m}^2$, $h_f = 30\ 000\ \text{W/(m}^2\ \text{K)}$, $T_f = 318.00°\text{C}$. The inverse analysis yields the values of unknown parameters: $q_m = 249\ 999.43\ \text{W/m}^2$, $h_f = 29\ 999.60\ \text{W/(m}^2\ \text{K)}$, $T_f = 318.00°\text{C}$, which are very close to the input values. The

http://dx.doi.org/10.5772/63807

reconstructed temperature distribution is shown in **Figure 12**. The uncertainty analysis was omitted because the results are very similar to the results obtained in Section 4.2.

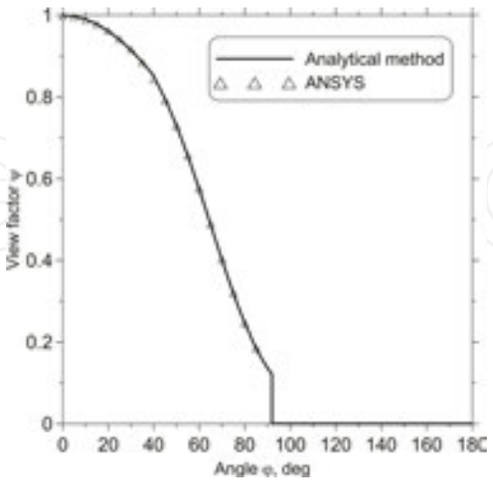


Figure 11. Comparison of view factor calculated analytically and by FEM for the flux tube shown in **Figure 2b**.

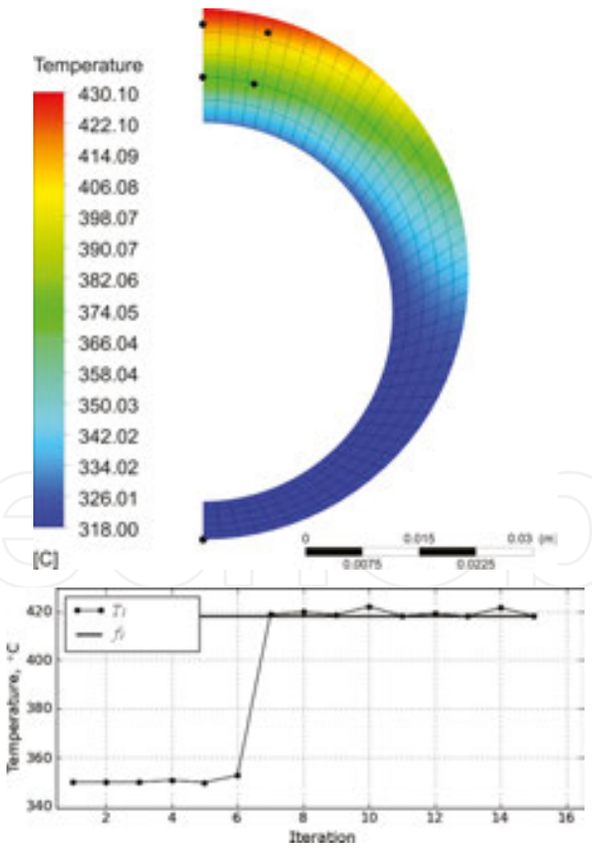


Figure 12. Temperature distribution in the flux tube obtained from the solution of the inverse problem for the unperturbed data: $f_1 = 418.28°C$, $f_2 = 415.61°C$, $f_3 = 374.05°C$, $f_4 = 372.18°C$, $f_5 = 318.00°C$; (a) temperature distribution; (b) iteration process.

2.5. Boiler test

The pulverized coal-fired boiler produces 58.3 kg/s superheated steam at 11 MPa and 540°C. Experimental studies were conducted in this boiler for a mass flow rate of live steam equal to $210 \cdot 10^3$kg/h. Measuring heat flux tubes were installed in the middle of the water wall at different levels of the boiler combustion chamber. Despite the boiler is operated in a steady state load, slow time variations in the measured temperatures are observed. This phenomenon is characteristic for the combustion of coal in large boilers. However, time changes of the meter temperature are very slow and the temperature distribution in the meter can be considered as a steady state. Temperature measurement results for the heat flux tubes located at a level of

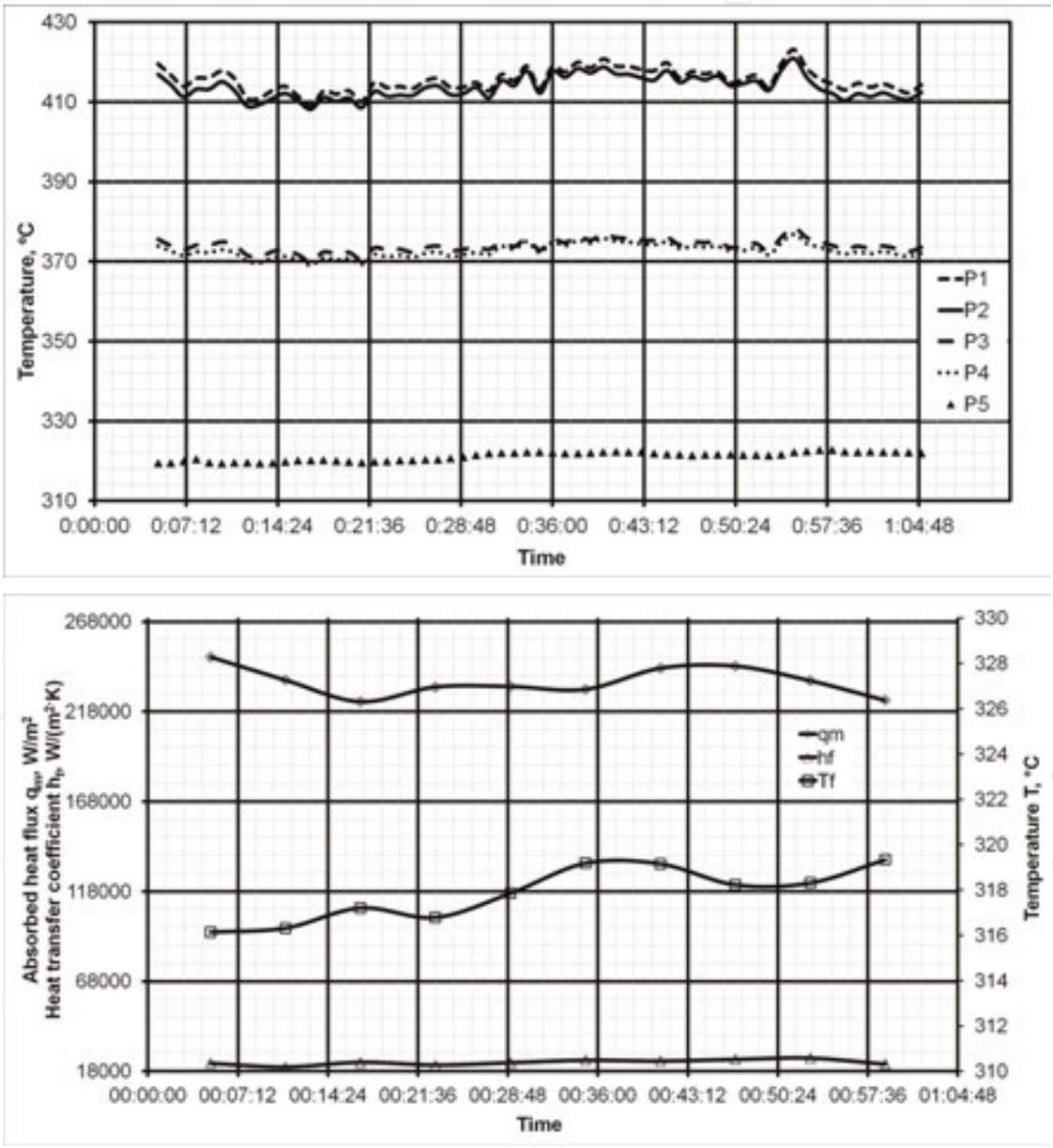


Figure 13. Measured temperature histories at five points for heat flux tube located at the level of 15.4 m (a) and estimated parameters: absorbed heat flux q_m. Heat transfer coefficient h_f and fluid temperature T_f (b).

15.4 m are depicted in **Figure 11a**, and the estimated parameters as functions of time are depicted in **Figure 11b**.

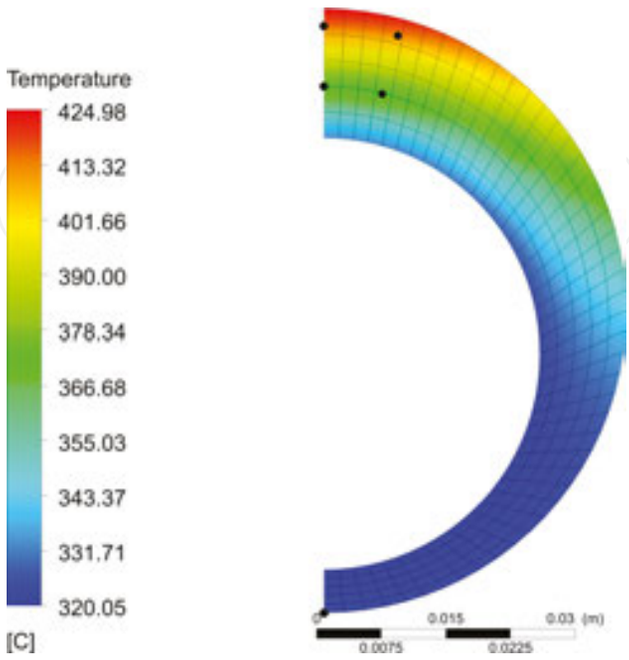


Figure 14. Temperature distribution in the cross section of the flux tube located at the level of 15.4 m. which was determined on the basis of measured temperatures: f_1 = 413.509°C; f_2 = 412.227°C; f_3 = 372.855°C; f_4 = 372.227°C; f_5 = 322.209°C. The estimated parameters are: q_m = 230425.8 W/m^2; h_f = 24128.8 W/(m^2 K); T_f = 319.19°C.

The differences between the measured and computed temperatures for the measurements at the elevation 15.4 m (**Figures 13a** and **14**) are reported in **Table 4**. The time points in the first column of **Table 4** are the same as indicated in **Figure 13a and b**.

Time	f_1, °C	T_1, °C	$f_1 - T_1$, K	f_2, °C	T_2, °C	$f_2 - T_2$, K	f_3, °C	T_3, °C	$f_3 - T_3$, K
00:05:00	419.55	419.58	−0.03	416.89	416.88	0.01	375.53	375.67	−0.15
00:11:00	415.87	415.76	0.11	412.85	413.19	−0.34	374.19	374.21	−0.02
00:17:00	408.98	409.76	−0.78	408.17	407.36	0.82	370.00	370.40	−0.40
00:23:00	413.61	413.79	−0.18	411.39	411.27	0.12	372.83	372.93	−0.10
00:29:00	413.74	414.16	−0.42	412.09	411.65	0.44	373.01	373.23	−0.22
00:35:00	413.51	414.09	−0.58	412.23	411.61	0.61	372.86	373.43	−0.57
00:41:00	418.98	419.28	−0.30	416.99	416.67	0.32	375.99	376.46	−0.47
00:47:00	417.67	418.30	−0.62	416.34	415.68	0.66	374.86	375.27	−0.41
00:53:00	413.76	414.56	−0.80	412.87	412.04	0.83	372.60	373.04	−0.44
00:59:00	413.05	412.94	0.10	410.38	410.51	−0.13	373.15	373.39	−0.24

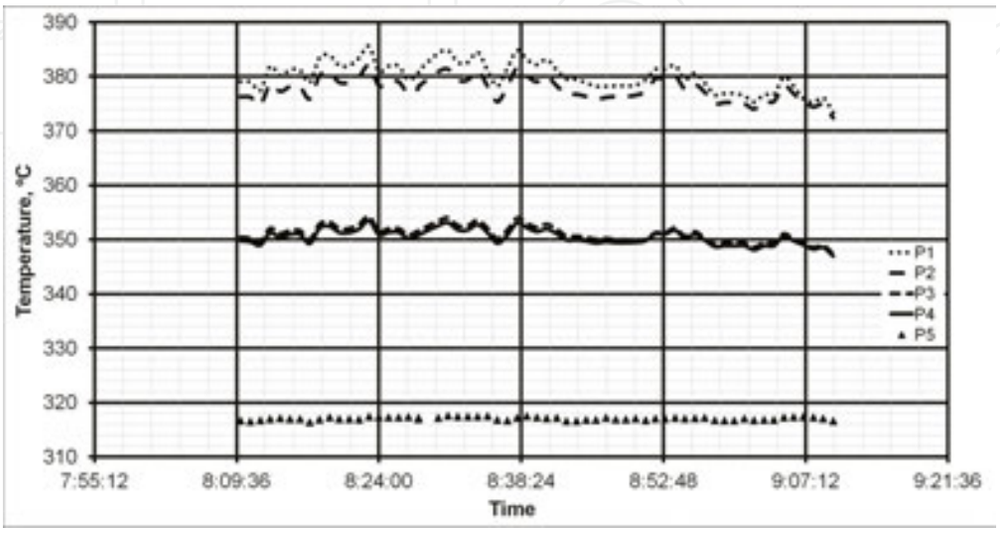
Time	f_4, °C	T_4, °C	f_4-T_4, K	f_5, °C	T_5, °C	f_5-T_5, K	S, K²
00:05:00	373.88	373.76	0.12	319.49	319.49	0.00	0.04
00:11:00	372.18	372.38	−0.19	319.60	319.60	0.00	0.17
00:17:00	369.06	368.69	0.38	320.18	320.20	−0.02	1.58
00:23:00	371.17	371.14	0.04	319.96	319.96	−0.01	0.06
00:29:00	371.66	371.45	0.21	320.96	320.98	−0.01	0.46
00:35:00	372.23	371.67	0.56	322.21	322.23	−0.02	1.35
00:41:00	375.06	374.61	0.46	322.36	322.38	−0.01	0.62
00:47:00	373.82	373.42	0.40	321.41	321.43	−0.02	1.14
00:53:00	371.67	371.26	0.42	321.36	321.38	−0.02	1.69
00:59:00	371.88	371.66	0.22	322.39	322.39	0.00	0.14

Table 4. The differences between measured and calculated temperatures.

The residuals and the sum of temperature difference squares are small. The obtained results show that the proposed method can be successfully applied to identify the operating conditions of water walls in boilers.

Similar measurements and calculations were performed for the insert located at a height of 19.2 m. The results of measurements and calculations are shown in **Figures 15** and **16**.

Measuring insert at an elevation of 15.4 m is situated directly above the burners which makes the value of absorbed heat flux q_m higher in comparison with the absorbed heat flux at a height of 19.2 m. At the level of 15.4 m, heat flux is approximately 230 000 W/m² while at the height of 19.2 m is about 168 000 W/m². It is worth mentioning a very high lifetime of measuring heat flux tubes, which is more than 5 years.



http://dx.doi.org/10.5772/63807

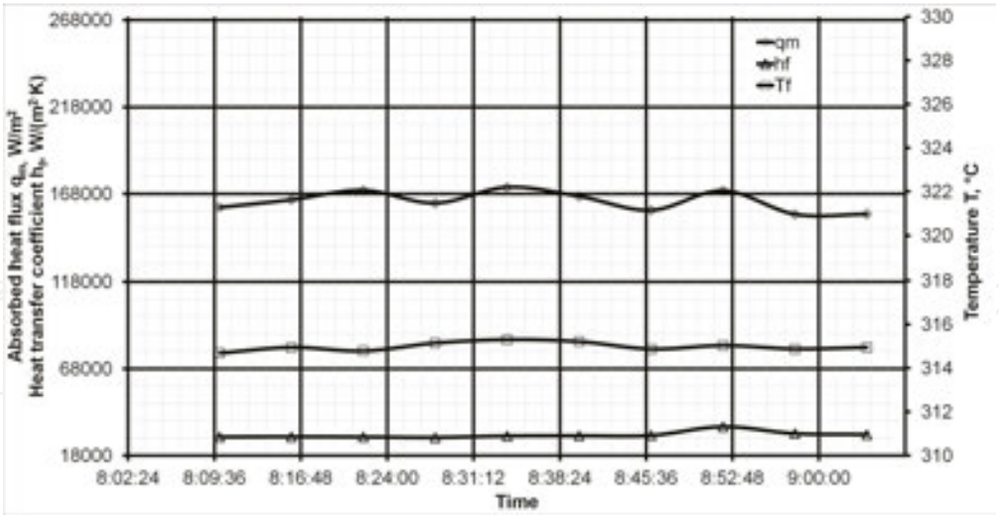


Figure 15. Measured temperature histories at five points for heat flux tube located at the level of 19.2 m (a) and estimated parameters: absorbed heat flux q_m heat transfer coefficient h_f and fluid temperature T_f (b).

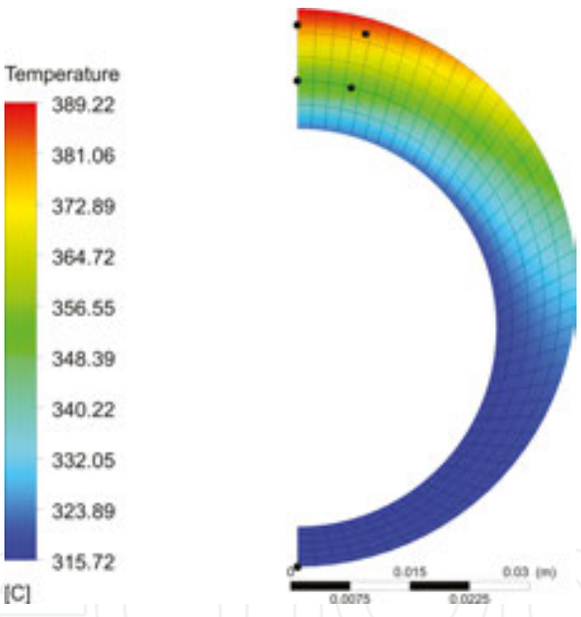


Figure 16. Temperature distribution in the cross section of the flux tube located at the level of 19.2 m. which was determined on the basis of measured temperatures: T_1 = 382.170°C; T_2 = 379.040°C; T_3 = 352.270°C; T_4 = 351.460°C; T_5 = 317.300°C. The estimated parameters are: q_m = 166 577.5 W/m²; h_f = 29 489.5 W/(m² K); T_f = 315.21°C.

3. Identification of thermal boundary conditions in heat exchangers of fluidized bed boilers

Circulating fluidized bed (CFB) boilers burning coal or biomass are in use for several years. Fluidized bed combustion is widely used in power boilers due to its impressive environmental

performance and also its fuel flexibility. Therefore, the studies of combustion and heat transfer are the subject of many recent investigations aimed at improving the design and operation of CFB boilers. Sun et al. [35] applied wide size biomass and investigated its combustion, heat transfer, and emission characteristics in CFB [35]. They found that co-firing wide screening crushed biomass pellets in CFB may reduce emissions and enhance heat transfer. Sundaresan and Kolar [36] conducted experiments to determine the total surface-average heat transfer coefficients from the tube to suspension for vertical tubes of different heights, which were placed in the core of a square cold CFB riser.

Superheaters and reheaters are the surfaces that achieve the highest temperatures in a boiler and for this reason require a lot of attention in the design, fabrication, operation, and maintenance to ensure that the permissible metal temperatures are never exceeded. A standard method for hydraulic calculation and design of boilers is described in [37]. The hydraulic calculation of superheater aims to provide the safe temperature of superheater tubes, efficient flow arrangement, and determination of pressure losses. Considerable attention has been given to hydraulic maldistribution in steam superheater tubes. A standard method for thermal design of steam boilers, including superheaters, was developed in [38]. Although the boiler standards are extensively used by manufacturers of boilers, they adopt for the calculation of the superheaters procedures which are used in design or performance calculations of usual heat exchangers assuming constant physical fluid properties [37–40]. For superheated steam, a constant value of the specific heat cannot be assumed because of the strong dependence on temperature. The specific heat of the water steam can decrease even twice over the length of the superheater tube.

The basic superheater and reheater design principles are discussed in detail by Rayaprolu [39]. Thermal and flow process in large steam boilers are the subject of the book [40]. Design and performance procedures for calculating of coal-fired boilers were described. Much attention has been paid to analyzing start-ups of steam boilers. Approximately 40% of all boiler failures are caused by damage of steam superheaters due to the overheating of the tube material [41]. Because of this, steam superheaters are modeled mathematically or monitored to avoid overheating of tubes. CFD simulations and optimization results of a 300 MW lignite-fired power boiler are presented by Tzolakis et al. [42]. A heat recovery steam generator (HRSG) was optimized by Behbahaninia using the genetic algorithm [43]. The results show that the thermodynamic optimization is not capable of decreasing significantly the total cost of the HRSG. Mathematical modeling of the boiler superheater was presented in not many publications despite a great interest of boiler manufacturers. This is mainly due to the difficulty of the description of complex flow and heat transfer processes taking place in the steam superheaters both in pulverized coal and fluidized boilers. A numerical method for modeling of the superheaters in pulverized coal-fired boilers was developed in [44, 45]. Much trouble causes the flue-gas temperature unevenness in a duct where a superheater is situated. A thermal load deviation model for the superheater and reheater in a utility boiler is presented by Xu et al. [46]. Many failure analyses on the superheaters were carried out to reveal the causes of tube overheating or tube rapture. The unevenness of the steam temperature is one of the main reasons for boiler tube failures. The 320 MW natural gas-fired boiler was simulated using the

CFD code by Rahimi et al. [47]. The main goal of the computational analysis was to detect the reason for the tube rupture inside the boiler. A new procedure for determining heat flux in superheater and reheater tubes based on the empirical formulas and the finite element modeling is presented by Purbolaksono et al. [48]. The finite element simulations were performed by Othman et al. [49] to find the main reason for superheater tube deformations. It was revealed that the failure of the tubes occurred due to the restriction of the tube deformations. Local short-term overheating of the tubes due to concentrated flue-gas flow was the primary cause of superheater tube failure [50]. A failure analysis was carried out using visual inspections and in situ measurements of hardness the experimental examination was supplemented by finite element analyzes. The rate of corrosive wear in superheaters of supercritical boilers was presented in the paper by Pronobis and Wojnar [51]. The slagging and fouling processes in superheaters influence the efficiency and lifetime of the boiler. Harding and O'Connor used the ten-year database to determine the lost generated through forced outages due to the coal quality or slagging and fouling issues [52]. A computer system for monitoring slagging and fouling of superheaters is described in [24].

Direct and inverse problems in a platen superheater situated in the combustion chamber of a CFB boiler were studied in [2].

The review of the state of the art in the field of superheaters shows that published papers on the superheaters present mostly experimental results and relate to search for the causes of failures of superheater tubes or analyze ash fouling.

In this work, the finite volume modeling of a platen superheater is presented. The fluidized bed boilers steam superheaters are placed in the combustion chamber and are made of tubes with non-circular cross sections, to avoid erosion and slagging (**Figure 17**). Due to the complex shape of the cross section of superheater tubes (**Figure 18**), numerical modeling has been applied to correctly determine the temperature distribution of steam and tube wall. Accurate calculating the superheater tube wall temperature is necessary because of the high prices of alloy steels used in superheater manufacturing.

A CFD simulation will be carried out for the platen superheater located in the combustion chamber of the CFB boiler. The second stage superheater is situated in the upper part of the combustion chamber of a circulating fluidized bed boiler (CFB boiler) with the capacity of 425 $\cdot 10^3$ kg/h steam. The steam boiler with a live steam temperature equal 560°C and a pressure of 16.1 MPa has an atmospheric circulating fluidized bed furnace. The superheater is a three-pass heat exchanger. The water steam flows inside the tubes while the flue gas with a constant temperature flows upwards in a perpendicular direction to the tube axes. Two inverse problems will be solved. First, the flue-gas side heat transfer coefficient h_g will be determined using temperatures measured at the outlet and inlet of the heat exchanger. This coefficient is essential for the proper design of superheaters in fluidized bed boilers. In the second inverse problem, in addition, to the heat transfer coefficient h_g will also be searched the steam temperature at the inlet to the superheater based on the measured steam temperatures at three points located at the ends of the superheater passes. Such inverse problem is encountered in a superheater steam temperature controllers.

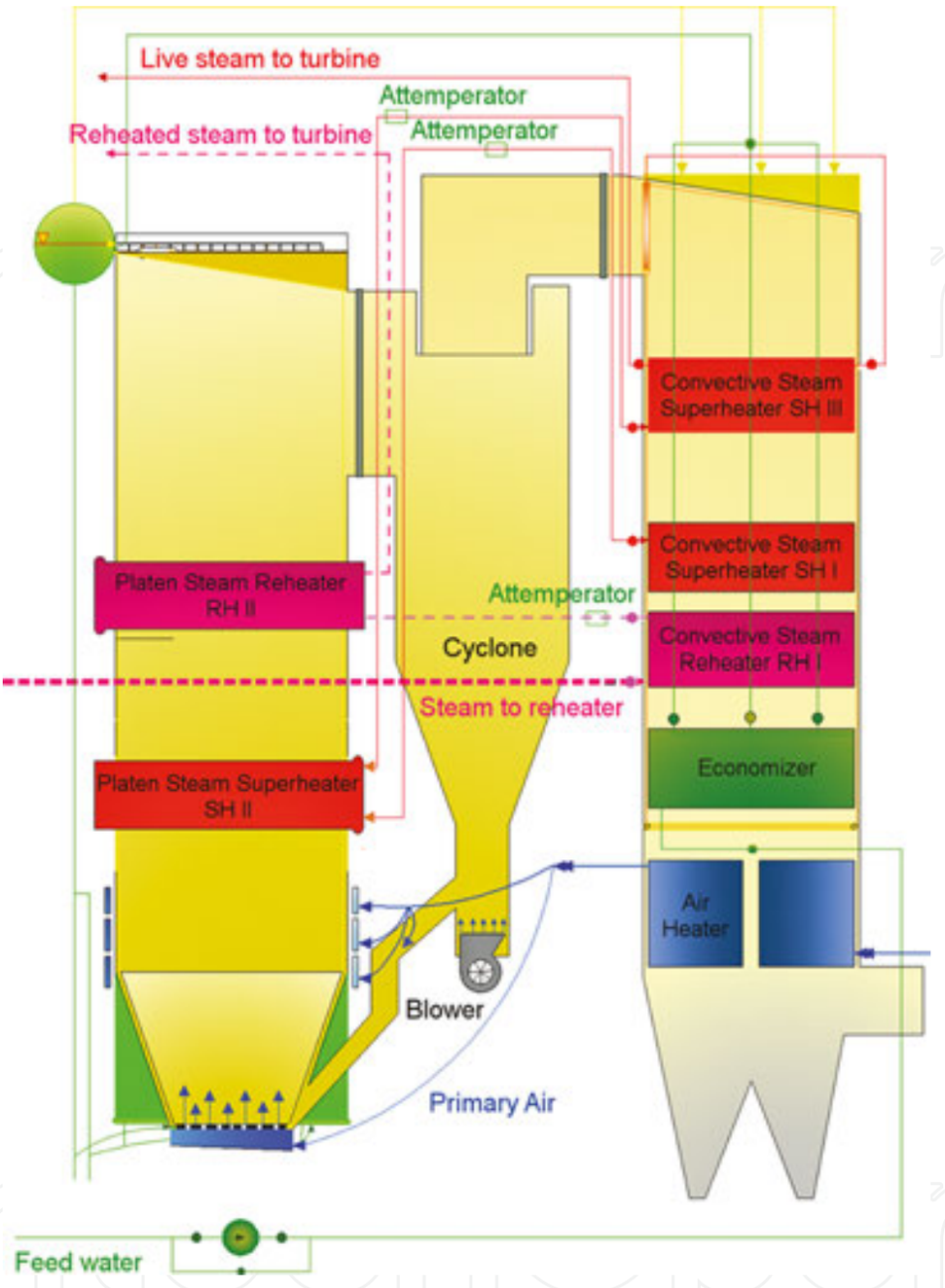


Figure 17. The arrangement of heating surfaces in circulating fluidized bed boiler with a steam capacity of $425 \cdot 10^3$ kg/h.

On modern large steam boilers, the temperature must be held close to design values since excessive temperatures have a serious effect on the metal lifetime of all parts of a boiler which are subject to it. The inlet steam temperature will be determined from the solution of the inverse problem. Based on this temperature, a correct flow rate of cooling water to the spray-type desuperheater (attemperator) is calculated. Despite the great practical importance, this type inverse heat transfer problems have not yet been analyzed.

http://dx.doi.org/10.5772/63807

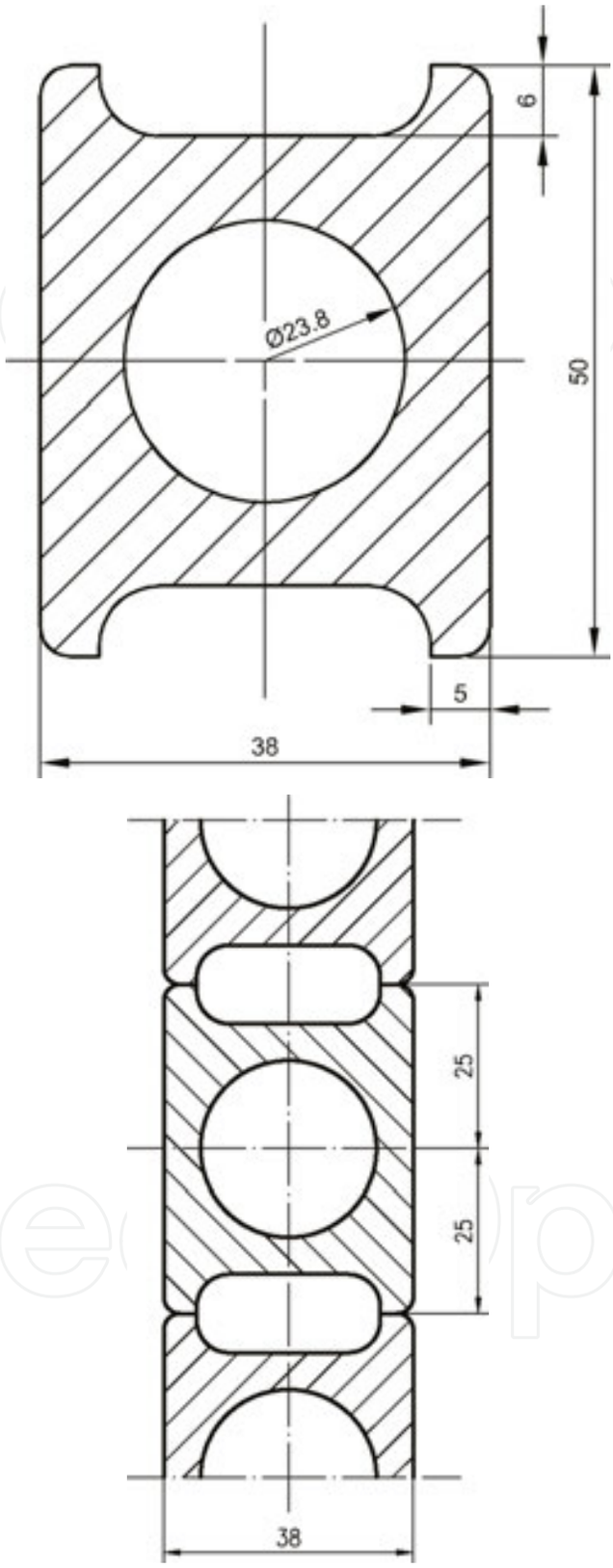


Figure 18. Platen superheater made from "omega" tubes; (a) cross section of omega tube, (b) platen superheater cross-section.

4. Description of the numerical method

Velocity, pressure, and temperature of the steam, as well as the temperature of the tube wall with the complex cross section, will be computed using the ANSYS/CFX v13.0 software [25].

The direct and inverse problems will be solved. In the inverse problem, the steam temperature at the superheater inlet and the heat transfer coefficient on the flue-gas side will be determined using measured steam temperatures at selected locations in the superheater. If the flue-gas side heat transfer coefficient is determined based on the measured steam temperature at the superheater outlet, the secant method is used. In this case, it is assumed that the inlet steam temperature is also measured. The Levenberg–Marquardt method is used to solve the least squares problem when the inlet steam temperature and the flue-gas side heat transfer coefficient are determined based on the measured steam temperature at the selected points along the steam flow path. At every iteration step, a direct problem was solved using the ANSYS/CFX v13.0 software. Time-averaged three-dimensional equations of conservation of mass, momentum and energy are solved using an element-based finite volume method. The heat transfer in the flowing steam was modeled using equations of mass, momentum, and energy conservation which can be written as follows [25]:

$$\frac{\partial \rho}{\partial t} + \nabla \cdot (\rho \mathbf{U}) = 0 \tag{19}$$

$$\frac{\partial (\rho \mathbf{U})}{\partial t} + \nabla \cdot (\rho \mathbf{U} \otimes \mathbf{U}) = -\nabla p + \nabla \cdot \tau + \mathbf{S_M} \tag{20}$$

$$\frac{\partial (\rho h)}{\partial t} - \frac{\partial p}{\partial t} + \nabla \cdot (\rho \, \mathbf{U} h) = \nabla \cdot (k \nabla T) + \mathbf{U} \cdot \nabla p + \tau : \nabla \mathbf{U} + \mathbf{S_E} \tag{21}$$

where the stress tensor τ is related to the strain rate by

$$\tau = \mu (\nabla \mathbf{U} + (\nabla \mathbf{U})^T - \frac{2}{3} \delta \nabla \cdot \mathbf{U}) \tag{22}$$

Temperature distribution in double omega tube walls (**Figure 18**) is governed by the heat conduction equation

$$c_w \rho_w \frac{\partial T_w}{\partial t} = \nabla \cdot [k_w (T_w) \nabla T_w] \tag{23}$$

http://dx.doi.org/10.5772/63807

Two equation turbulence model SST (Shear Stress Transport), which was developed based on the Wilcox *k*–*ω* and *k*–*ε* turbulence models [53], was used to model the flow turbulence. The baseline *k*–*ω* model is a two equations turbulence model that offers a good compromise between numerical effectiveness and computational accuracy. This model is a combination of the *k*–*ω* and *k*–*ε* models.

The Wilcox *k*–*ω* model is given by two equations:

$$\frac{\partial(\rho k)}{\partial t}+\frac{\partial}{\partial x_j}\left(\rho U_j k\right)=\frac{\partial}{\partial x_j}\left[\left(\mu+\frac{\mu_t}{\sigma_{k1}}\right)\frac{\partial k}{\partial x_j}\right]+P_k-\beta'\rho k\omega \tag{24}$$

$$\frac{\partial(\rho\omega)}{\partial t}+\frac{\partial}{\partial x_j}\left(\rho U_j \omega\right)=\frac{\partial}{\partial x_j}\left[\left(\mu+\frac{\mu_t}{\sigma_{\varpi 1}}\right)\frac{\partial \omega}{\partial x_j}\right]+\alpha_1\frac{\omega}{k}P_k-\beta_1'\rho\omega^2 \tag{25}$$

To develop the baseline *k*–*ω* turbulence model, the transformed *k*–*ε* model is also used:

$$\frac{\partial(\rho k)}{\partial t}+\frac{\partial}{\partial x_j}\left(\rho U_j k\right)=\frac{\partial}{\partial x_j}\left[\left(\mu+\frac{\mu_t}{\sigma_{k2}}\right)\frac{\partial k}{\partial x_j}\right]+P_k-\beta'\rho k\omega \tag{26}$$

$$\begin{aligned}&\frac{\partial(\rho\omega)}{\partial t}+\frac{\partial}{\partial x_j}(\rho U_j\omega)=\\&=\frac{\partial}{\partial x_j}\left[\left(\mu+\frac{\mu_t}{\sigma_{\varpi 2}}\right)\frac{\partial \omega}{\partial x_j}\right]+2\rho\frac{1}{\sigma_{\varpi 2}\omega}\frac{\partial k}{\partial x_j}\frac{\partial \omega}{\partial x_j}+\alpha_2\frac{\omega}{k}P_k-\beta_2\rho\omega^2\end{aligned} \tag{27}$$

Multiplying Eqs. (24) and (25) of the Wilcox model by weighting function F_1, the transformed *k*–*ε* Eqs. (26) and (27) by a weighting function $(1 - F_1)$ and adding the transformed equations gives the baseline *k*–*ω* model:

$$\frac{\partial(\rho k)}{\partial t}+\frac{\partial}{\partial x_j}(\rho U_j k)=\frac{\partial}{\partial x_j}\left[\left(\mu+\frac{\mu_t}{\sigma_{k3}}\right)\frac{\partial k}{\partial x_j}\right]+P_k-\beta'\rho k\omega+P_{kb} \tag{28}$$

$$\begin{aligned}&\frac{\partial(\rho\omega)}{\partial t}+\frac{\partial}{\partial x_j}(\rho U_j\omega)=\\&=\frac{\partial}{\partial x_j}\left[\left(\mu+\frac{\mu_t}{\sigma_{\omega 3}}\right)\frac{\partial \omega}{\partial x_j}\right]+\left(1-F_1\right)2\rho\frac{1}{\sigma_{\omega 2}\omega}\frac{\partial k}{\partial x_j}\frac{\partial \omega}{\partial x_j}+\alpha_3\frac{\omega}{k}P_k-\beta_3\rho\omega^2+P_{\omega b}\end{aligned} \tag{29}$$

The baseline k–ω model has the advantages of the Wilcox k–ω, and the k–ε but is not able to predict onset and amount of flow separation from smooth surfaces [53]. The main reason for this drawback is neglecting of the transport of the turbulent shear stress. This causes an over-prediction of the eddy-viscosity. In order to eliminate this deficiency, the shear stress transport (SST) turbulence model was developed [53], in which the turbulent viscosity ν_t is limited by the following equation:

$$\nu_t = \frac{\alpha_1 k}{\max(\alpha_1 \omega, SF_2)} \tag{30}$$

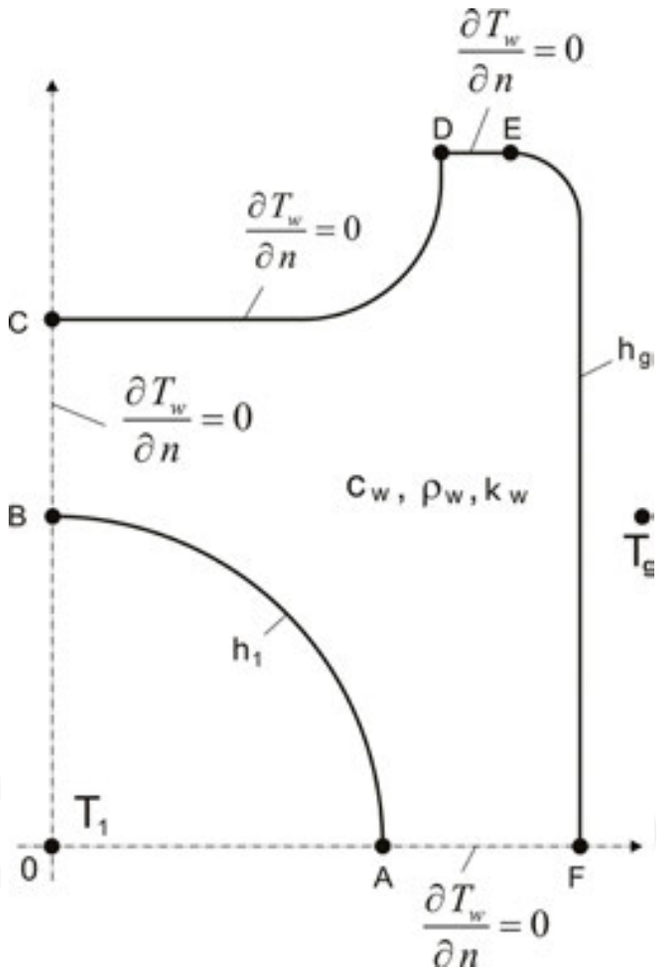


Figure 19. One-fourth of a tube cross section.

Because of the symmetry, only one-fourth of a tube cross section was analyzed (**Figure 19**). Heat is transferred by convection from the combustion chamber to the tube through the surface E–F. The surfaces A–F and B–C–D–E are thermally insulated. The tube inner surface A–B is cooled by the flowing live steam. The following boundary conditions were assumed for the tube wall (**Figure 19**):

http://dx.doi.org/10.5772/63807

$$T|_{A-B} = T_w|_{A-B}, \quad k\,\frac{\partial T}{\partial n}|_{A-B} = -k_w\,\frac{\partial T_w}{\partial n}|_{A-B} \tag{31}$$

$$k_w\,\frac{\partial T_w}{\partial n}|_{B-C-D-E} = 0 \tag{32}$$

$$k_w\,\frac{\partial T_w}{\partial n}|_{E-F} = h_g\,(T_g - T_w|_{E-F}) \tag{33}$$

$$k_w\,\frac{\partial T_w}{\partial n}|_{A-F} = 0 \tag{34}$$

Also, the fluid temperature and the steam mass flow rate or steam velocity are known at the inlet of the tube. The steam pressure is given at the outlet of the tube. The direct conjugate heat transfer problem described by Eqs. (19) and (29) with appropriate boundary conditions was solved using the ANSYS/CFX software.

5. Results of the superheater modeling using ANSYS//CFX

The ANSYS CFX commercial software v13.0 [25] was used for the numerical calculations. Computer calculations were carried out for the second stage of the steam superheater which is made of omega tubes from 10CrMo 910 low alloy steel. At first, direct and inverse problems were solved for the single tube representing the first pass of the superheater. A finite element mesh contains 1 233 999 elements and 747 945 finite element nodes. The cross section of the tube is shown in **Figure 18**. The length of the modeled tube is 8 517 mm. Thermal properties of the superheated steam were calculated using the industrial standard IAPWS-IF97 [54]. Changes in thermal conductivity with temperature for the 10CrMo 910 steel are shown in **Figure 20**.

At first, test simulations were performed for the following data:

- T_{in} = 462°C—temperature of the superheated steam at tube inlet,
- P_{out} = 16.5 MPa—pressure of the steam at tube outlet,
- T_g = 850°C—flue-gas temperature in the combustion chamber,
- h_g = 200 W/(m^2 K)—heat transfer coefficient on the gas side.

Two different steam inlet velocities u_{in}: 16.7 m/s and 10 m/s were assumed at the inlet of the tube to illustrate the influence of the steam side conditions on the steam and tube wall

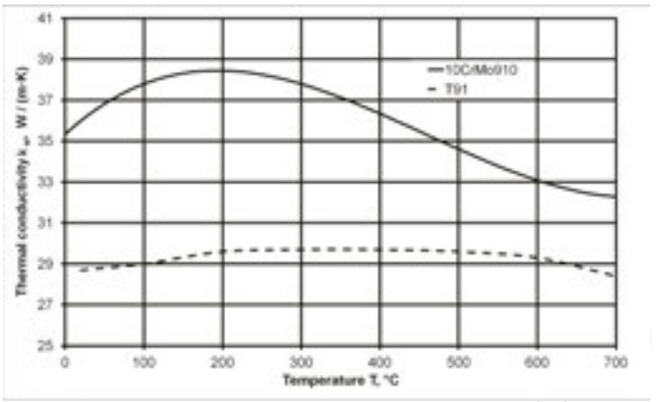


Figure 20. The thermal conductivity of 10CrMo 910 and T91 steels as a function of temperature.

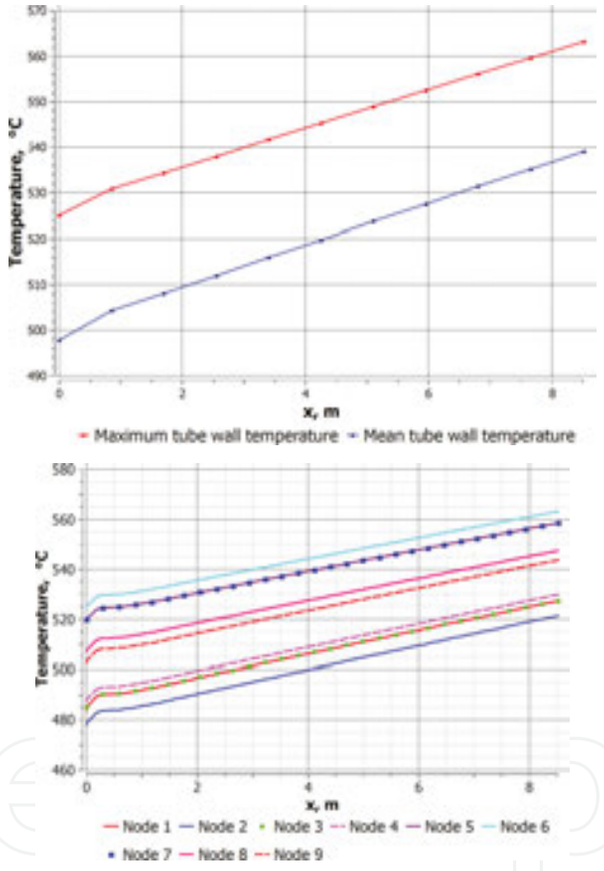


Figure 21. Tube wall temperature; (a) changes of mean and maximum tube wall temperature over the tube length, (b) temperature of the tube wall at the nodes: 1, 2, 3, 4, 5, 7, 8, and 9 over the tube length; u_{in} = 16.7 m/s, h_g = 200 W/(m^2 K).

temperature. The steam velocity of 16.7 m/s corresponds to 100% boiler load, while the steam velocity equal to 10 m/s corresponds to the partial boiler load. Then, to assess the impact of the gas side heat transfer coefficient h_g on the temperature of the steam and tube, calculations for u_{in} = 16.7 m/s and h_g = 250 W/(m^2 K) were also carried out.

The results of the computer simulation for u_{in} = 16.7 m/s and h_g = 200 W/(m^2 K) are shown in **Figures 21–23**.

http://dx.doi.org/10.5772/63807

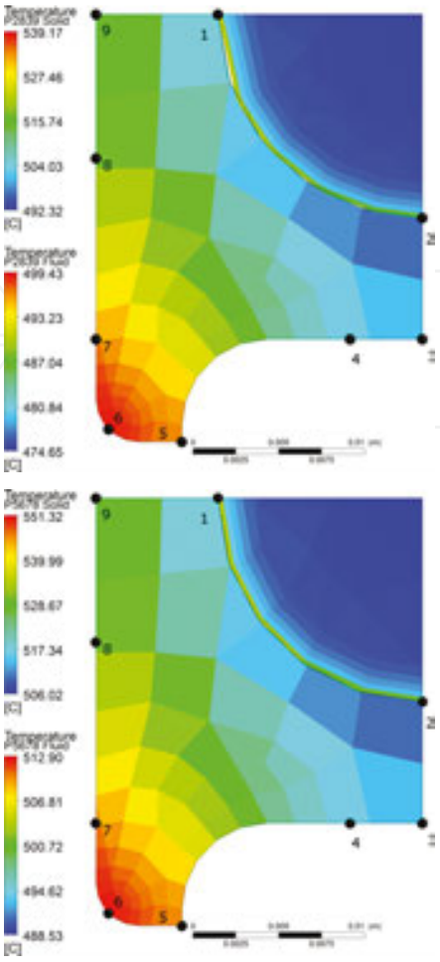


Figure 22. The temperature distribution in the tube wall and steam in two cross sections; (a) at the distance of 2839 mm from the inlet; (b) at the distance of 5678 mm from the inlet; u_{in} = 16.7 m/s, h_g = 200 W/(m^2 K).

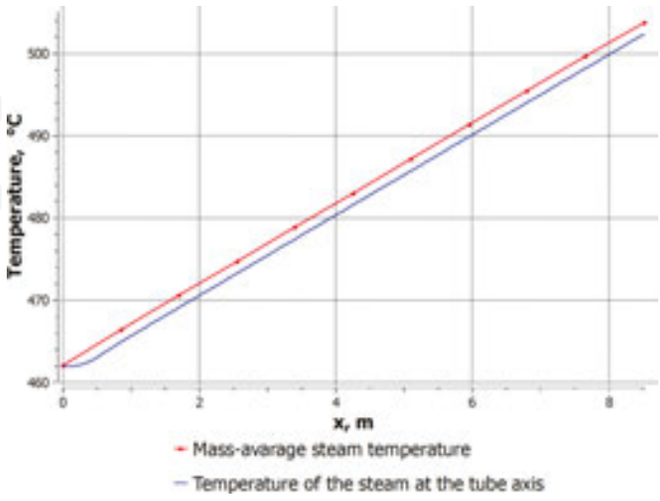


Figure 23. Mass-average steam temperature and the temperature of the steam at the tube axis.

From the analysis of the results shown in **Figure 21a** and **b**, it can be seen that the steam temperature over the tube length grows almost linearly. Only, in the region close to the tube inlet the wall temperature is lower. This is due to much higher heat transfer coefficient in the developing flow which occurs at the inlet region of the tube. The steam in the boundary layer is cool at the inlet section, which contributes to a better cooling tube wall. It should be noted that the difference between the maximum and average temperature over the tube cross section is large but does not exceed 30 K (**Figure 21a**).

The rise of the tube wall temperature is almost linear over a length of the tube due to the constant value of the heat transfer coefficient in the region of the developed flow. At the entrance section of the tube, the heat transfer coefficient is higher because of developing a fluid flow. In this region, the temperature difference over the boundary layer is greater, so the heat flux and heat transfer coefficient are larger, and tube temperature is lower. **Figures 22a** and **6b** show the temperature distribution in the tube wall and steam at two cross sections away from the inlet, respectively at the distance of 2 839 mm and 5 678 mm. The maximum temperature of the wall is at the tube edge (**Figure 22a**). This temperature is 539.2°C at the distance of 2 839 mm and 551.3°C at the distance of 5678 mm from the inlet of the tube. The increase of the mass-average steam temperature over the entire length of the tube is 41 K (**Figure 23**).

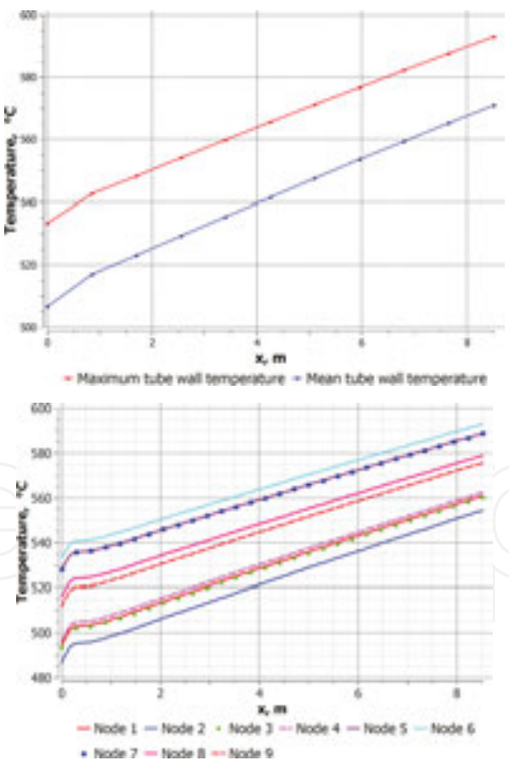


Figure 24. Tube wall temperature; (a) changes of mean and maximum tube wall temperature over the tube length, (b) temperature of the tube wall at the nodes: 1, 2, 3, 4, 5, 7, 8, and 9 over the tube length; u_{in} = 10 m/s, h_g = 200 W/(m^2 K).

The value obtained from the numerical simulation is in good agreement with the measured rise in the steam temperature. Steam temperature is highest near the inner surface of the tube.

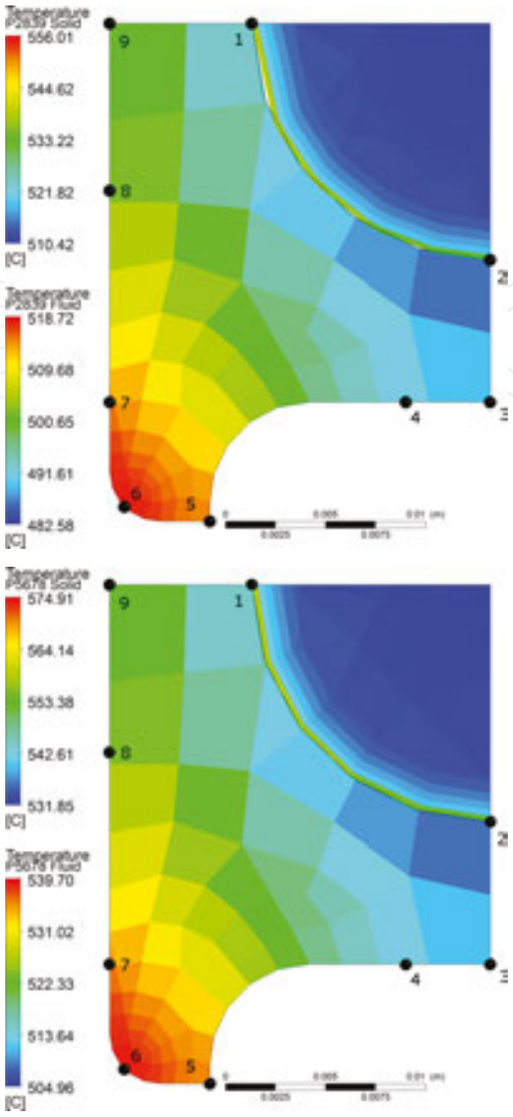


Figure 25. The temperature distribution in the tube wall and steam in two cross sections; (a) at the distance of 2839 mm from the inlet; (b) at the distance of 5678 mm from the inlet; u_{in} = 10 m/s, h_g = 200 W/(m²·K).

For the two different steam velocities at the inlet to the pipe: 16.7 m/s and 10 m/s the difference between the mass-average temperature of the steam and temperature in the axis of the tube is small (**Figure 23**). Tube wall temperatures are higher when the steam velocity at the inlet is lower and equal to u_{in} = 10 m/s. The results of the computer simulation for u_{in} = 10 m/s and h_g = 200 W/(m² K) are shown in **Figures 24** and **25**. A similar effect on the tube wall temperature has the heat transfer coefficient on the flue-gas side. The CFD simulation was thus performed for the velocity of the steam at the tube inlet: u_{in} = 16.7 m/s and the heat transfer coefficient on the gas side: h_g = 250 W/(m² K), that is, the heat transfer coefficient was increased by 50 W/(m² K). The CFD simulation results are shown in **Figures 26** and **27**. If the heat transfer coefficient on the gas side is h_g = 250 W/(m² K) then the steam and tube wall temperature is higher, because the heat flow rate transferred from flue gas to the steam is larger (**Figures 26** and **27**).

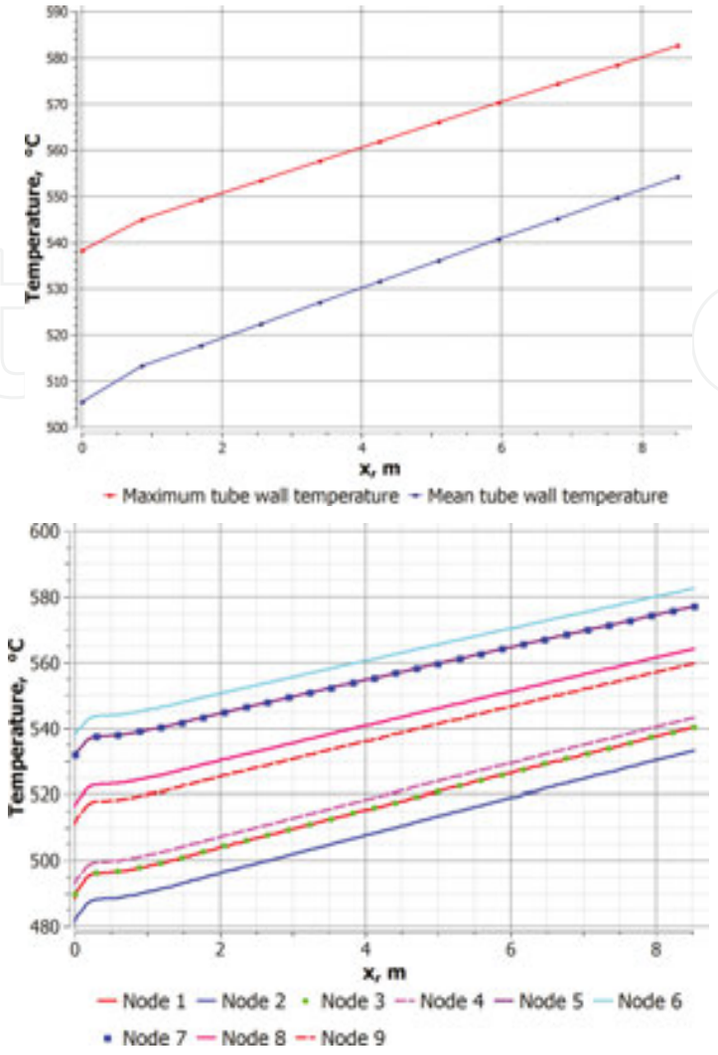
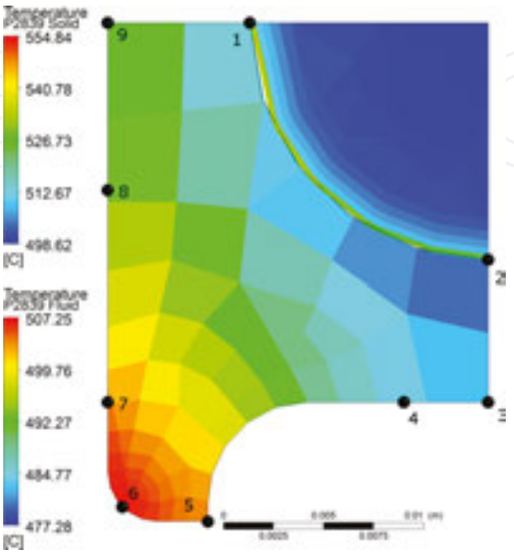


Figure 26. Tube wall temperature; (a) changes of mean and maximum tube wall temperature over the tube length, (b) temperature of the tube wall at the nodes: 1, 2, 3, 4, 5, 7, 8, and 9 over the tube length; u_{in} = 16.7 m/s, h_g = 250 W/(m^2 K).



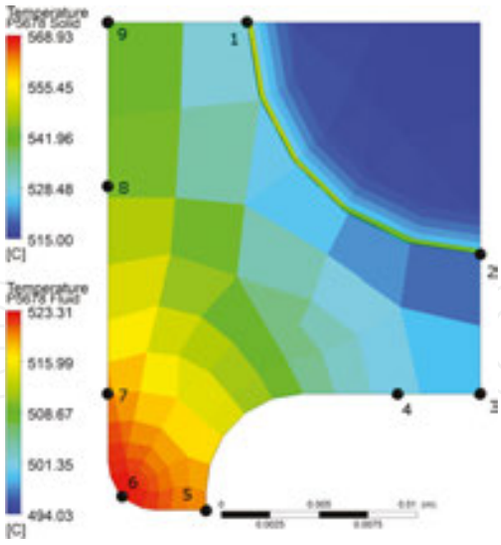


Figure 27. The temperature distribution in the tube wall and steam in two cross sections; (a) at the distance of 2839 mm from the inlet; (b) at the distance of 5678 mm from the inlet; u_{in} = 16.7 m/s, h_g = 250 W/(m^2 K).

The correctness of the results obtained using CFD simulation was examined using the energy balance equation. The heat flow rate $\dot{Q}_{out}$ transmitted through the outer surface of the tube with an area of A_{out}, which is given by the integral

$$\dot{Q}_{out} = \int_{A_{out}} \dot{q}_{out} dA \tag{35}$$

should be equal to the heat flow rate $\dot{Q}_{in}$ transmitted through the inner surface

$$\dot{Q}_{in} = \int_{A_{in}} \dot{q}_{in} dA \tag{36}$$

and to the heat flow rate $\dot{Q}_s$ absorbed by the steam

$$\dot{Q}_s = \dot{m}(h_{outlet} - h_{inlet}) \tag{37}$$

where h_{inlet} and h_{oulet} stand for the steam enthalpy at the inlet and the outlet of the superheater tube, respectively, and $\dot{m}$ denotes the steam mass flow rate. The symbols $\dot{q}_{out}$ and $\dot{q}_{in}$ designate the heat flux at the outer and inner tube surface. It has been proved that the solution is independent of the finite volume mesh. Twelve different meshes were examined. The finite element number ranged from 790 179 to 3 789 699. For the CFD simulations presented in the work, the mesh consisting of 1 233 999 elements with the total number of nodes equal to 747 945 was selected. The quality requirements for the finite element mesh, given in the CFX

Reference Guide, were satisfied. The mesh statistics like the orthogonal angle, expansion factor, and aspect ratio were confirmed by the CFX solver that they are correct [25].

For the analyzed case: $u_{in} = 16.7$ m/s, $h_g = 200$ W/(m^2 K) and for the mesh consisting of 1 233 999 elements, the following values of the heat flow rate were obtained:

$$\dot{Q}_{out} = \dot{Q}_{in} = = 57.266\,\text{kW and } 57.644\,\text{kW}.$$

The relative difference defined as:

$$\varepsilon_Q = \frac{0.5(\dot{Q}_{in} + \dot{Q}_{out}) - \dot{Q}_s}{0.5(\dot{Q}_{in} + \dot{Q}_{out})} 100, \%$$

is: $\varepsilon_Q = -0.656\%$

If the number of elements was increased to 3 789 699, then the relative difference is almost the same and equal to: $\varepsilon_Q = -0.655\%$.

The consistency of the results is very good. Taking into account that in the inverse problem is solved iteratively, the direct problem is repeatedly solved so the element mesh cannot be too fine because of computing time.

6. Inverse problem

Ten platens of the superheater SH II are located at combustion chamber of the circulating fluidized bed boiler (**Figure 17**). Steam temperature is measured outside of the combustion chamber at the points 1–4. Because these points are located outside of a fire region, it is easy to measure steam temperature by attaching the thermocouple to the tube outer surface that is thermally insulated (**Figure 28**).

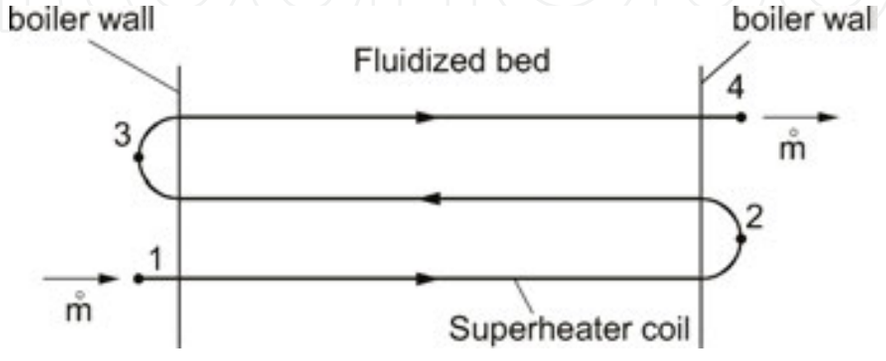


Figure 28. Three pass single superheater coil.

http://dx.doi.org/10.5772/63807

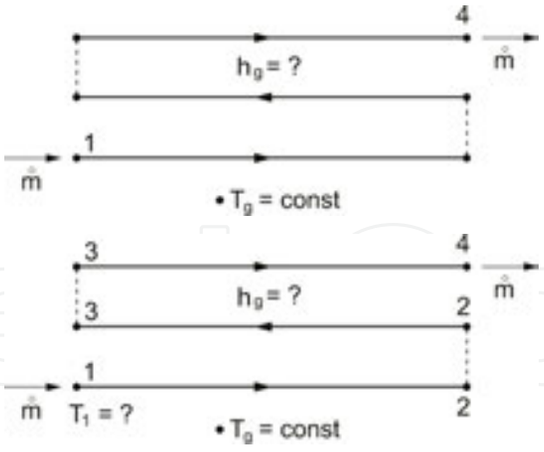


Figure 29. Inverse problem for a three pass second stage platen superheater, (a) flue-gas side heat transfer coefficient α_g is determined based on steam temperature measured at point number 4, (b) flue-gas side heat transfer coefficient h_g and inlet steam temperature T_1 are determined based on steam temperature measured at points 2, 3, and 4.

No.	Input data					Results	
	$\dot{m}$, kg/s	T_g, °C	P_4, MPa	f_1, °C	f_4, °C	α_g, W/(m²K)	P_1, MPa
1	0.2644	812.7	8.73	366.54	508.45	115.54	8.82
2	0.3148	826.78	10.12	379.35	505.74	123.83	10.22
3	0.4616	866.11	13.71	393.79	501.04	160.59	13.86

Table 5. Input data and results for the first inverse problem (**Figure 27a**).

Two different inverse problems were solved. The first and second inverse problems are presented in **Figure 29a** and **b**, respectively. At first, a flue-gas side heat transfer coefficient h_g was estimated based on the measured steam temperature at the outlet and at the end of the three pass platen superheater made from omega tubes with the length of 8517 mm (**Figure 29b**). Also flue-gas temperature T_g, steam mass flow rate $\dot{m}$ per one tube, and the outlet steam pressure P_4 are known from measurements **Figure 27a**. The inverse problem was solved for three data sets (**Table 5**). The heat transfer coefficient h_g was adjusted to obtain the outlet steam temperature T_4 equal to the measured value f_4. The following nonlinear algebraic equation

$$T_4 - f_4 = 0 \tag{38}$$

was solved iteratively using the secant method [27, 28] to determine the flue-gas side heat transfer coefficient h_g. At every iteration step, the temperature distribution in the tube wall and steam was determined using ANSYS/CFX. The three pass steam superheater was divided into finite element mesh which has 3 603 132 finite elements and 2 207 434 nodes (**Figure 30**). The solution of the inverse problem (**Table 6**) was obtained only after a few iterations. The CFD

simulation also enabled the determination of pressure P_1 at the inlet to the superheater (**Table 5**).

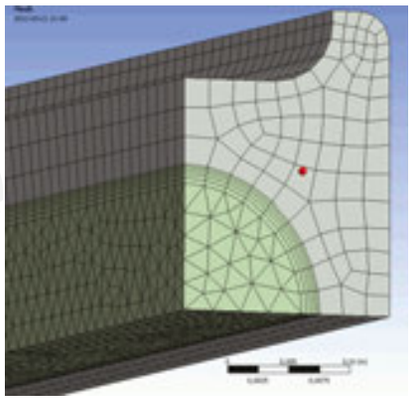


Figure 30. Finite volume mesh for a tube quarter.

No.	Input data						Results		
	$\dot{m}$, kg/s	T_g, °C	P_4, MPa	f_2, °C	f_3, °C	f_4, °C	h_g, W/(m²·K)	T_1, °C	P_1, MPa
1	0.2644	812.70	8.73	414.89	463.02	508.45	114.95	365.66	8.82
2	0.3148	826.78	10.12	422.43	464.00	505,74	121.65	379.68	10.22
3	0.4616	866.11	13.71	427.88	463.65	501.04	158.81	393.54	13.85

Table 6. Input data and results for the second inverse problem (**Figure 29b**).

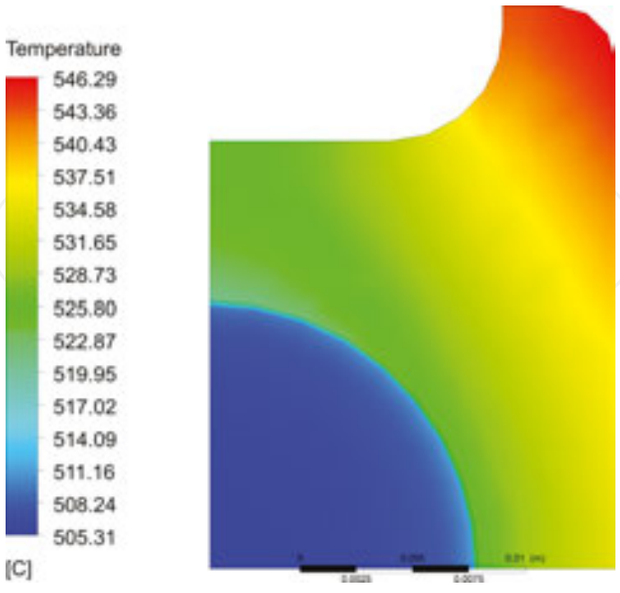


Figure 31. Steam and tube wall temperature distribution at the outlet of the three pass superheater for the data set number 1—three measurement points (**Table 6**).

http://dx.doi.org/10.5772/63807

In the second inverse problem, the flue-gas side heat transfer coefficient $x_1 = h_g$ and steam temperature $x_2 = T_1$ at the inlet of the superheater are two unknowns which were determined based on measured steam temperatures f_2, f_3, and f_4 at three points 2, 3, and 4 located at the outlets of each pass (**Figure 29b**). The number of measured temperatures is greater than the number of unknown parameters to increase the accuracy of the solution of the inverse problem. If the number of measuring points is greater, then the effect of random errors in temperature measurements on the results obtained from the solution of the inverse problem is smaller.

The least-squares method was used to determine parameters h_g and T_1. The sum of squares

$$S = \sum_{i=2}^{4} (f_i - T_i)^2 \tag{39}$$

was minimized using the Levenberg–Marquardt method [26]. At every k-th iteration step, the steam temperature distribution $\mathbf{T}(\mathbf{x}^{(k)}, \mathbf{r}_i)$ is calculated, where $\mathbf{r}_i$designates the position vector of the steam measurements points. The steam and tube wall temperature were calculated at each iteration step using ANSYS/CFX software. The CFX program was called and controlled by an external program written in Python language [28]. The Levenberg–Marquardt algorithm was also included in the Python program. Three data sets were used in the inverse analysis (**Table 6**). From the analysis of the results shown in **Table 7**, it can be seen that the agreement between the calculated and measured steam temperature at the superheater inlet is very satisfactory. Also, the minimum value of the sum of squared temperature differences (39) is very small (**Table 7**). The similar values of the heat transfer coefficients h_g were obtained from the solution of the first and second inverse problems (**Tables 5** and **7**).

The actual measured data were adopted for the inverse analysis: tube material—T91 steel, pass length—8517 mm. The thermal conductivity of T91 steel as a function of temperature is shown in **Figure 20**. The experimental data sets adopted for the inverse analysis and the estimated heat transfer coefficients α_g and steam inlet temperatures $T>_1$ are shown in **Table 6**. The computed temperatures at the measurement locations are very close to the measured values (**Table 7**). The minimum sum of the temperature difference squares is small.

The analysis of the results listed in **Table 7** shows that steam temperature increase is almost the same in each pass. Despite the decreasing temperature difference between the flue gas and steam the increases in steam temperature are: $(T_2 - T_1) = 42.51$ K, $(T_3 - T_2) = 42.31$ K, and $(T_4 - T_3) = 40.98$ K for the first, second, and third pass, respectively (**Table 7**, data set no. 2). The reason for this is a large reduction in the specific heat of the steam with the temperature. To achieve the same steam temperature rise in the third pass, much less heat flow rate is needed in comparison with the first pass.

The uncertainties of the determined parameters $\mathbf{x}^*$ were estimated using the error propagation rule of Gauss [29–33]. The propagation of uncertainty in the independent variables, that is, in measured steam temperatures f_2, f_3, and f_4, is estimated from the following equation:

$$2\sigma_{x_i} = \left[\sum_{j=2}^{m} \left(\frac{\partial x_i}{\partial f_j} 2\sigma_{f_j} \right)^2 \right]^{\frac{1}{2}}, \quad m = 4, \quad i = 1,2 \tag{40}$$

The 95% uncertainty in the estimated parameters can be expressed in the form $x_i = x_i^* \pm \sigma_{x_i}$, where $x_i = x^*_i$, i=1, 2, 3 represent the value of the parameters obtained using the least squares method.

Assuming that the 95% uncertainty in measured steam temperatures is equal $2\sigma_{fj}$ = 0.5 K for j = 2, 3, 4 the uncertainties in calculated temperature T_1 and heat transfer coefficient h_g are: $2\sigma_{T_1}$ = 0.74 K and $2\sigma_{h_g}$ = 0.99 W/(m^{2}K). The results are quite satisfactory.

No.	f_1, °C	f_2, °C	f_3, °C	f_4, °C	$e = \frac{f_1 - T_1}{f_1} \cdot 100$, %	S_{min}, K^2
	T_1, °C	T_2, °C	T_3, °C	T_4, °C		
1	366.54	414.89	463.02	508.45	0.240	0.0006
	365.66	414.88	463.04	508.44		
2	379.35	422.43	464.00	505.74	−0.087	0.3752
	379.68	422.19	464.50	505.48		
3	393.79	427.88	463.65	501.04	0.064	0.0384

Table 7. Comparison of measured and calculated steam temperatures at the inlet to the superheater and at measuring points 3, 4, and 5.

7. Conclusions

The chapter presents an effective method for solving nonlinear inverse heat transfer problems using CFD software. Application of the method is illustrated by the identification of the boundary conditions in water wall tubes and boundary conditions in a platen superheater of a CFB boiler.

A CFD-based method for determining heat flux absorbed by water-wall tubes, heat transfer coefficient at the inner flux-tube surface and temperature of the water-steam mixture has been presented. New heat flux tubes were proposed. The flux tubes are not welded to the adjacent water-wall tubes, so the temperature distribution in the measuring device is not affected by neighboring water-wall tubes. Based on the measured flux-tube temperatures the nonlinear inverse heat conduction problem was solved. The number of thermocouples placed inside the heat flux tube including the thermocouple on the rear outer tube surface is greater than the number of unknown parameters because additional measurement points reduce the uncertainty in determined parameters. To achieve a good accuracy of measurements, the uncer-

http://dx.doi.org/10.5772/63807

tainties in measured heat flux-tube temperatures and the radial thermocouple locations should be small since they have the largest impact on the accuracy of the parameter estimation. The proposed flux tubes and the inverse procedure for determining absorbed heat flux can be used both when the inner surface of the heat flux tube is clean and when the scale or corrosion deposits are present on the inner surface what can occur after a long time service of the heat flux tube. The flux tubes can work for a long time in the destructive high-temperature atmosphere of a coal-fired boiler.

The CFD simulation of the thermal-hydraulic processes occurring in the platen steam superheater, located in the combustion chamber of the fluidized bed boiler, was carried out.

The temperature distributions in the tube wall of complex shape and the flowing steam were computed. The steam velocity and pressure distributions can be determined with high accuracy. The CFD modeling is a useful tool to explore the real fluid and heat flow phenomena which occur in platen superheaters operating at high thermal loads. It is well known that even a small increase in tube operating temperature over the design temperature will reduce stress rapture life significantly. The CFD simulation allows calculation of the maximum tube wall temperature along the steam flow path for complex cross section shape of the tubes and complicated flow arrangement of the superheater. The detailed CFD prediction makes possible the proper selection of the steel grade for the analyzed superheater stage or superheater pass.

The temperature-dependent physical properties of the steam and tube material can be easily taken into account. The specific heat of water steam decreases significantly with increasing temperature. The calculations show that the temperature rise in each of the three passes is almost the same in spite of decreasing the temperature difference between the flue gas and steam. If the specific heat were constant, the steam temperature increase in the third pass would be much smaller compared to the first pass. It should be stressed, that it would be impossible to calculate accurately the steam and tube wall temperature if the classical methods for heat exchanger calculations, which assume constant physical steam properties, were used.

Accurate calculation of the heat transfer coefficient on the flue-gas side of the platen superheater placed in the boiler furnace is critical for boiler design. The inaccurate calculation of the heat transfer coefficient is the reason for tubes damage due to an excessive steam temperature which frequently happens in power plants. A new method for determining of the flue-gas side heat transfer coefficient was developed.

The flue-gas side heat transfer coefficient or the inlet steam temperature and flue-gas side heat transfer coefficient were determined based on the measured steam temperatures at selected points along the steam flow path. To solve the inverse problems, the secant method was used when only one temperature measurement point was applied, and one unknown, that is, the heat transfer coefficient on the flue-gas side was searched. The Levenberg–Marquardt method was used to solve the over-determined heat transfer problem. For the solution of the direct conjugate heat transfer problem, which is encountered at every iteration step, while the inverse problem is being solved, ANSYS/CFX software was used.

Identifying the flue-gas side heat transfer coefficients for various boiler loads using the inverse method, a simple mathematical model of the platen superheater can be developed and used in the control system of the superheated steam temperature.

The proposed method of solution can be successfully applied to solve other inverse problems occurring in industrial practice.

Nomenclature

c_w	specific heat capacity, J/(kg K)
f_i	*i*-th measured steam temperature, K or °C
F	weighting function
F_2	blending function
h	specific enthalpy, J/kg
h_1, h_g	heat transfer coefficient on the inner and outer tube surface, W/(m^2 K)
$\mathbf{I}$	identity matrix
$\mathbf{J}$	Jacobian matrix
k	turbulence kinetic energy, m^2/s^2
k_w	tube wall thermal conductivity, W/(m K)
m	number of temperature measurements points
$\dot{m}$	steam mass flow rate, kg/s
n	outward normal, m
n	number of unknowns parameters
p	pressure, Pa
P_k	production rate of turbulence energy, kg/(m s^3)
P_ω	turbulent frequency production term, s/m^2
$\dot{q}$	heat flux, W/m^2
$\dot{Q}$	heat flow rate, W/m^3
r	radius, m
S	invariant measure of the strain rate, 1/s
$\mathbf{S}_E$	energy source, kg/(m s^3)
$\mathbf{S}_M$	momentum source, kg/(m^2 s^2)
t	time, s
T	fluid temperature, K or °C
T_g	flue-gas temperature
T_w	tube wall temperature, K or °C
u	steam velocity, m/s
$\mathbf{U}$	vector of velocity

U_j	j-th velocity component
x, y, z	Cartesian coordinates
x_1,x_2,x_3	unknown parameters
x_j	jth coordinate

Greek letters

α,β,β'	model constant in the Wilcox k-ω turbulence model
δ	identity matrix
ε	turbulence eddy dissipation, m^2/s^3
μ	dynamic viscosity, kg/(m·s)
μ_t	turbulent dynamic viscosity, kg/(m·s)
ν_t	turbulent kinematic viscosity, m^2/s
ρ	density, kg/m^3
ρ_w	tube wall density, kg/m^3
σ	standard deviation
σ_k	turbulence model constant in kinetic energy equation
σ_ω>	k-ω turbulence model constant
τ	stress tensor
Ω	turbulent frequency, 1/s
∇	gradient operator (nabla)
$\otimes$	dyadic operator (tensor product)

Author details

Paweł Ludowski[1*], Dawid Taler[2] and Jan Taler[3]

*Address all correspondence to: pawel.ludowski@gmail.com

1 ABB Corporate Research Center, Cracow, Poland

2 Institute of Thermal Engineering and Air Protection, Cracow University of Technology, Cracow, Poland

3 Institute of Thermal Power Engineering, Cracow University of Technology, Cracow, Poland

References

[1] Taler J, Taler D, Ludowski P. Measurements of local heat flux to membrane water walls of combustion chambers. Fuel 2014;115:70–83.

[2] Ludowski P, Taler D, Taler J. Identification of thermal boundary conditions in heat exchangers of fluidized bed boilers. Appl Therm Eng 2013;58:194–204

[3] Shimogori M, Mine T, Ohyatsu N, Takarayama N, Matsumura Y. Effects of fine ash particles and alkali metals on ash deposition characteristics at the initial stage of ash deposition determined in 1.5 MWth pilot plant tests. Fuel 2012;97:233–240.

[4] Vainikka P, Enestam S, Silvennoinen J, Taipale R, Yrjas P, Frantsi A, Hannula J, Hupa M. Bromine as an ash forming element in a fluidised bed boiler combusting solid recovered fuel. Fuel 2012;90:1101–1112.

[5] Liang Q, Guo X, Dai Z, Liu H, Gong X. An investigation on the heat transfer behavior and slag deposition of membrane wall in pilot-scale entrained-flow gasifier. Fuel 2012;102:491–498.

[6] Moghari M, Hosseini S, Shokouhmand H, Sharifi H, Izadpanah S. A numerical study on thermal behavior of a D-type water-cooled steam boiler. Appl Therm Eng 2012;37:360–372.

[7] Taler J, Duda P, Węglowski B, Zima W, Grądziel S, Sobota T, Taler D. Identification of local heat flux to membrane water-walls in steam boilers. Fuel 2009;88:305–311.

[8] Duda P, Taler J. A new method for identification of thermal boundary conditions in water wall tubes. Int J Heat Mass Transf 2009;52:1517–1524.

[9] Beckmann M, Krüger S. Online heat flux measurement at membrane walls of steam generators of municipal solid waste incinerators. In: Proceedings of the 24th Annual International Conference on Incineration and Thermal Treatment Technologies, IT3 Conference, Galveston, Texas, USA, May 9–13, 2005. College Park: University of Maryland; 2005, p. 1–18.

[10] Krüger S., Measurement of heat flux in steam generators, Dresden University of Technology, Faculty of Mechanical Engineering 978-3-935317-41-2. Neuruppin: TK Verlag Karl Thomé-Kozmiensky; 2009.

[11] Taler J, Taler D. Measurement of heat flux and heat transfer coefficient in heat flux processes. In: Cirimele G, D'Elia M, editors, Heat flux: processes, measurement techniques and applications, New York: Nova Science Publishers; 2012, p. 1–103.

[12] Seeger M, Taler J. Design and application of portable heat flux probes for measuring of specific thermal load in combustion chambers of steam boilers. Fortschr.-Ber. VDI Zeitschrift. Reihe 6. Nr 129. Düsseldorf: VDI-Verlag; 1983.

[13] Northover EW, Hitchcock JA. A heat flux meter for use in boiler furnaces. J Sci Instrum 1967;44:371–374.

[14] Neal SBHC, Northover EW. The measurement of radiant heat flux in large boiler furnaces-I. Problems of ash deposition relating to heat flux. Int J Heat Mass Transf 1980;23:1015–1022.

[15] Arai N, Matsunami A, Churchill SW. A review of measurements of heat flux density applicable to the field of combustion. Exp Therm Fluid Sci 1996;12:452–460.

[16] Taler J. Measurement of heat flux to steam boiler membrane water walls. VGB Kraftwerkstechnik 1990;70:540–546.

[17] Taler J. A method of determining local heat flux in boiler furnaces. Int J Heat Mass Transf 1992;35:1625–1634.

[18] Fang Z, Xie D, Diao N, Grace JR, Jim Lim C. A new method for solving the inverse conduction problem in steady heat flux measurement. Int J Heat Mass Transf 1997;40:3947–3953.

[19] Luan W, Bowen BD, Lim CJ, Brereton CMH, Grace JR. Suspension-to membrane-wall heat transfer in a circulating fluidized bed combustor. Int J Heat Mass Transf 2000;43:1173–1185.

[20] Sobota T, Taler D. The measurement of radiant heat flux in combustion chambers of large steam boilers. In: 8th World Congress on Computational Mechanics (WCCM8) and 5th European Congress on Computational Methods in Applied Sciences and Engineering (ECCOMAS 2008). Venice. June/July. 2008.

[21] Sobota T, Taler D. A simple method for measuring heat flux in boiler furnaces. Rynek Energii 2010;86:108–114.

[22] Valero A, Cortes C. Ash fouling in coal-fired utility boilers. Monitoring and optimization of on-load cleaning. Prog Energy Combust Sci 1996;22:189–200.

[23] Teruel E, Cortes C, Diez LI, Arauzo I. Monitoring and prediction of fouling in coal-fired utility boilers using neural networks. Chem Eng Sci 2005;60:5035–5048.

[24] Taler J, Trojan M, Taler D. Monitoring of ash fouling and internal scale deposits in pulverized coal fired boilers. In: Malach DE, editor. Advances in mechanical engineering research, Volume 1, New York: Nova Science Publishers; 2011, p. 91–131.

[25] ANSYS CFX 13. ANSYS Inc. Urbana. Illinois. USA. 2010.

[26] Marquardt W. An algorithm for least-squares estimation of nonlinear parameters. J Soc Ind Appl Math, 1963;11(2):431–441.

[27] Press WH, Teukolsky SA, Vetterling WT, Flannery BP. Numerical recipes in Fortran. The art of scientific computing. New York: Cambridge University Press; 2006.

[28] Kiusalaas J, Numerical methods in engineering with Python. second ed. New York: Cambridge University Press; 2010.

[29] ISO. Guide to the expression of uncertainty in measurement. Geneva: International Organization for Standardization; 1993.

[30] Moffat R. ASME Policy on reporting uncertainties in experimental measurements and results. ASME Heat Transf 2000;122:411–413.

[31] Bevington PR. Data reduction and error analysis for the physical sciences. New York: McGraw-Hill; 1969.

[32] Brandt S. Data analysis. Statistical and computational methods for scientists and engineers. 3rd ed. Berlin: Springer; 1999.

[33] Coleman HW, Steele WG. Experimentation, validation, and uncertainty analysis for engineers. 3rd ed. Hoboken: Wiley; 2009.

[34] Richter F. Temperature-dependent physical properties of steels. Düsseldorf: Mannesmann Forschungberichte 930; 1983.

[35] Sun P, Hui S, Gao Z, Zhou Q, Tan H, Zhao Q, Xu T. Experimental investigation on the combustion and heat transfer characteristics of wide size biomass co-firing in 0.2 MW circulating fluidized bed. Appl Therm Eng 2013;52:284–292.

[36] Sundaresan R, Kolar A K. Axial heat transfer correlations in a circulating fluidized bed riser, Appl Therm Eng 2013;50:985–996.

[37] Lokshin V A, Peterson D F, Schwarz A L. Standard Methods of Hydraulic Design for Power Boilers, Hemisphere, Washington, USA, 1988.

[38] Kuznetsov N W, Mitor W W, Dubovski I E, Karasina E S. (editors), Thermal Calculations of Steam Boilers (Standard Method), Second edition, Energia, Moscow, Russia, 1973.

[39] Rayaprolu R. Boiler for power and process, CRC Press-Taylor & Francis Group, Boca–Raton, USA, 2009.

[40] Taler J (Editor). Thermal and flow processes in large steam boilers, Modeling and monitoring, PWN, Warsaw, Poland, 2011 (in Polish).

[41] French DN. Metallurgical failures in fossil fired boilers, second ed., John Wiley & Sons, New York, USA, 1993.

[42] Tzolakis G, Papanikolaou P, Kolokotronis D, Samaras N, Tourlidakis A, Tomboulides A. Simulation of a coal-fired power plant using mathematical programming algorithms in order to optimize its efficiency. Appl Therm Eng 2012;48:256–267.

[43] Behbahani-nia A, Bagheri M, Bahrampoury R. Optimization of the fire tube heat recovery steam generators for cogeneration plants through genetic algorithm. Appl Therm Eng 2010;30:2378–2385.

[44] Taler D, Trojan M, Taler J. Mathematical modeling of cross-flow tube exchangers with the complex flow arrangement. Heat Transf Eng 2014; 11–12 (11–12).

[45] Trojan M, Taler D. Thermal simulation of superheaters taking into account the processes occurring on the side of the steam and flue gas. Fuel 2015;150: 75–87.

[46] Xu L, Khan J A, Chen Z. Thermal load deviation model for superheater and reheater of a utility boiler. Appl Therm Eng 2000;20:545–558.

[47] Rahimi M, Khoshhal A, Shariati S M. CFD modeling of a boiler's tubes rupture. Appl Therm Eng 2006;26:2192–2200.

[48] Purbolaksono J, Khinani A, Rashid AZ, Ali AA, Ahmad J, Nordin BF. A new method for estimating heat flux in superheater and reheater tubes. Nucl Eng Des 2009;239:1879–1884.

[49] Othman H, Purbolaksono J, Ahmad B, Failure investigation on deformed superheater tubes. Eng Fail Anal 2009;16:329–339.

[50] Purbolaksono J, Ahmad J, Beng LC, Rashid AZ, Khinani A, Ali AA. Failure analysis on a primary superheater tube of a power plant. Eng Fail Anal 2010;17: 158–167.

[51] Pronobis M, Wojnar W. The rate of corrosive wear in superheaters of boilers for supercritical parameters of steam. Eng Fail Anal 2012;19:1–12.

[52] Harding NS, O'Connor DC. Ash deposition impacts in the power industry. Fuel Process Technol 2007;88:1082–1093.

[53] Menter FR. Two-equation eddy-viscosity turbulence models for engineering applications. AIAA J 1994;32:1598–1605.

[54] Wagner W, Kretzschmar HJ. International steam tables-properties of water and steam based on the industrial formulation IAPWS-IF97. Berlin. Springer Press. 2008

IntechOpen

IntechOpen

IntechOpen